

Synchro-curvature description of γ -ray light curves and spectra of pulsars: concurrent fitting

Daniel Íñiguez-Pascual^{1,2*}, Diego F. Torres^{1,2,3†}, Daniele Viganò^{1,2,4‡}

¹*Institute of Space Sciences (ICE, CSIC), Campus UAB, Carrer de Can Magrans s/n, 08193 Barcelona, Spain*

²*Institut d'Estudis Espacials de Catalunya (IEEC), 08034 Barcelona, Spain*

³*Institució Catalana de Recerca i Estudis Avançats (ICREA), E-08010 Barcelona, Spain*

⁴*Institute of Applied Computing & Community Code (IAC3), University of the Balearic Islands, Palma, 07122, Spain*

3 April 2025

ABSTRACT

We present a concurrent fitting of spectra and light curves of the whole population of detected gamma-ray pulsars. Using a synchro-curvature model we compare our theoretical output with the observational data published in the Third Fermi Pulsar Catalog, which has significantly increased the number of known gamma-ray pulsars. Our model properly fits all the spectra and reproduces well a considerable fraction of light curves. Light curve fitting is carried out with two different techniques, whose strong points and caveats are discussed. We use a weighted reduced χ^2 of light curves in time domain, and the Euclidean distance of the Fourier transform of the light curves, i.e. transforming the light curves to the frequency domain. The performance of both methods is found to be qualitatively similar, but individual best-fit solutions may differ. We also show that, in our model based on few effective parameters, the light curve fitting is basically insensitive to the timing and spectral parameters of the pulsar. Finally, we look for correlations between model and physical parameters, and recover trends found in previous studies but without any significant correlation involving geometrical parameters.

Key words: pulsars: general – gamma-rays: stars – X-rays: stars – acceleration of particles – radiation mechanisms: non-thermal

1 INTRODUCTION

The population of detected gamma-ray pulsars has been greatly enlarged by the recent release of the Third Fermi Pulsar Catalog (Smith et al. 2023), hereafter referred to as 3PC, containing data for 294 objects¹. A recognizable feature of the 3PC is the quality of the gamma-ray light curves presented. Comparison of these observational light curves with synthetic ones generated by theoretical models can provide relevant information about the structure of pulsars magnetospheres, for instance about the production sites of high-energy radiation. This task has been addressed widely in the last 20 years, either considering gap models (Watters et al. 2009; Romani & Watters 2010; Venter et al. 2009; Pierbattista et al. 2015), force-free electrodynamics (Bai & Spitkovsky 2010; Kalapotharakos et al. 2014; Cao & Yang 2019; Benli et al. 2021; Pétri & Mitra 2021) or Particle-in-Cell (PIC) magnetospheric simulations (Philippov & Spitkovsky 2018; Kalapotharakos et al. 2018). Each of these approaches focus on different aspects of pulsar physics, and their versatility,

computational cost, and physics included in the models differ from one another, see Philippov & Kramer (2022) for a review.

Very recently, Cerutti et al. (2024) has used PIC simulations to fit the light curves of the 3PC, with promising results. We shall compare our results with this paper in more detail below. Only few studies exist producing together gamma-ray light curves and spectra of pulsars (Cerutti et al. 2016; Pétri 2019; Kalapotharakos et al. 2023) and even less comparing those with observational data (Chang et al. 2019; Yang & Cao 2024).

In this paper we present a concurrent fitting of spectra and light curves for the whole population of objects quoted in the 3PC. We follow the spectral fitting from our previous works (Viganò et al. 2015b; Torres et al. 2019; Íñiguez-Pascual et al. 2022a), and here we mostly focus on the light curve fitting. The latter is performed with two different techniques that we scrutinize in detail, i.e. using a weighted, reduced χ^2 to assess the goodness of the light curve fits in time domain or using the Euclidean distance in frequency domain by comparing the Fourier transform of both the observational and synthetic light curves. Section 2 presents a brief summary of the spectral and geometrical models that generate the high-energy spectra and light curves. The comparison of theoretical spectra with observational ones is shown in Section 3. The light curve fitting procedures are discussed in Section

* E-mail: iniguez@ice.csic.es

† E-mail: dtorres@ice.csic.es

‡ E-mail: vigan@ice.csic.es

¹ https://fermi.gsfc.nasa.gov/ssc/data/access/lat/3rd_PSR_catalog/

4, and the results shown in Section 5. We also consider how well a single pulsar can describe the whole light curve variety, despite being generated in systems with different timing and spectral properties. Finally, in Section 6 we draw the main conclusions.

2 SYNCHRO-CURVATURE MODEL

The synchro-curvature model we use in this work has been extensively studied in a series of papers before (Viganò & Torres 2015; Viganò et al. 2015b; Torres 2018; Torres et al. 2019; Viganò & Torres 2019; Íñiguez-Pascual et al. 2022a,b, 2024). In this set of papers, among other things, we enlarged the energy coverage from gamma to X-rays, included better descriptions of the emission regions, studied how well the spectra can be used to infer the pulsar periods. Here we are not presenting additional theoretical improvement of the spectral model and thus, we will just give a very brief summary, referring the reader to these works for more details.

The model follows the dynamics of a bunch of charged particles moving in the magnetosphere of a pulsar, outside the light cylinder, whose motion is described by the equation of motion of charged particles. Having the strength of the electric field component parallel to the magnetic field E_{\parallel} and the magnetic gradient b as free model parameters, we numerically solve the equation of motion and use the synchro-curvature formulae to obtain the emission of a single particle at each position λ (Cheng & Zhang 1996; Viganò et al. 2015a), $dP_{sc}(\lambda)/dE$, which is then convolved with a relative weight given to the particle distribution, $dN/d\lambda$, ruled by a lengthscale x_0 , which is the third free parameter of our spectral model. These three parameters, plus a normalization factor N_0 that is fixed by observational comparison, fully describe the total radiation emitted by a pulsar with a particular P and \dot{P} , referred to as dP_{tot}/dE as in Eq. (7) of Íñiguez-Pascual et al. (2022a).

Together with the dynamics and emission of the emitting particles, we also compute the geometry of the trajectories they follow. In Viganò & Torres (2019) and Íñiguez-Pascual et al. (2024) we presented how to obtain the emission directions of the particles on the emission region, whose shape is given by Eq. (2) of Íñiguez-Pascual et al. (2024). Notice that by emitting region we mean the whole set of particle trajectories considered to be generating the radiation. For a fixed set of spectral parameters, collecting these emission directions in a sphere centered at the neutron star we build energy-dependent synchro-curvature emission maps, or simply, skymaps, which we refer to as $M_E(\theta_{obs}, \phi_{\Omega}, E)$ as in Equation 5 of Íñiguez-Pascual et al. (2024). This represents the photon flux received by a given observer at a given phase and energy, per unit energy, per unit solid angle, emitted by particles injected all along the region. In these skymaps, the x-axis corresponds to the rotational phase of the neutron star ϕ_{Ω} and the y-axis is the viewing angle θ_{obs} , the angle between the plane perpendicular to the rotational axis of the neutron star and the line-of-sight of an observer detecting the pulsar. By symmetry on the region definition, calculations are symmetric around the equatorial observer. For a given pulsar, skymaps are mostly determined by the inclination angle, ψ_{Ω} , the angle between the rotational and magnetic axes. In this work we consider the emission integrated over the Fermi

energy range, 100 MeV – 300 GeV, for the sake of a direct comparison with data. The emission maps within this range don't vary much with energy, and we leave the comparison between different sub-ranges for a future work. The synthetic, discrete light curve, for a given viewing angle θ_{obs} is then defined as: $I(\phi_{\Omega}) = \int_{E_{min}}^{E_{max}} M_E(\theta_{obs}, \phi_{\Omega}, E) dE$.

For a given pulsar with period P and period derivative \dot{P} , we find the parameters E_{\parallel}, b, x_0 which better fit the phase-averaged spectrum (including X-ray data, if available) as in our previous studies, and then look for the values of ψ_{Ω} and θ_{obs} which best fit the Fermi light curve.

3 FITTING OBSERVATIONAL SPECTRA

3.1 Sample selection

Out of the 294 gamma-ray pulsars presented on the 3PC, there is a fraction that is currently not eligible for fitting. This happens either because the pulsars lack a measured \dot{P} , or because their spectra are described with too few data points. With regards to the latter, we only consider fitable pulsars those having 5 consecutive bins with a measured flux (not upper limits) in their spectra. In this way, the fitting sample consists of 129 pulsars, 39 of them having also detected X-ray pulsations, the same sample studied in Coti Zelati et al. (2020).

Even though spectra of many previously unknown gamma-ray pulsar have been released in the 3PC, a dedicated spectral analysis to each pulsar on the catalog has not been performed yet. The spectra given in the catalog relate to those published in the Incremental Fermi-LAT Fourth Source Catalog (Abdollahi et al. 2022). For this reason, in some pulsars the spectral data on the 3PC may be less detailed than that publicly available before its release, coming either from Abdo et al. (2013) (hereafter 2PC), where a dedicated spectral analysis for each pulsar was done, or in dedicated studies of particular pulsars.

Therefore, we do not take the whole sample of spectra directly from the 3PC, but instead do a mix between those and the spectral data we used in Íñiguez-Pascual et al. (2022a), explicitly stating the origin of the data in a case-by-case basis. For the new pulsars we obviously take the 3PC data. For those with already-available data, we decide between the spectra from the 3PC or the older ones (meaning 2PC or dedicated studies) based on their quality and following the criterion of having at least 5 consecutive bins with a measured flux (i.e. not upper limits). In pulsars for which it is not immediately obvious which set to pick, we choose the data providing the largest number of consecutive data points, always checking that the overall shape between the sets is similar and/or that their difference lies within the errors. For these pulsars we consider systematic errors on the best-fit parameters (being the difference between the best-fit parameters obtained with the 3PC observational spectra and the alternative spectra) in addition to the statistical ones. In a few cases, the spectra of the two sets of data differ widely. We do not consider these pulsars in our systematic fitting, but show them in Appendix A. They are interesting candidates for further study and the light curves are mostly unaffected (see below) by spectral changes.

3.2 Results

The spectral fitting procedure we have followed in this work is the same as that in [Íñiguez-Pascual et al. \(2022a\)](#), and we refer the reader there for more details. For each pulsar we let our free spectral parameters to vary and search for the best set of parameters by minimizing the reduced χ^2 . For pulsars with available X-ray data the three parameters ($E_{||}$, b , x_0) are let free, while for those pulsars having only gamma-ray data, the magnetic gradient b is fixed to 2.5, since this parameter has a low impact in the gamma-ray band and mainly affects the X-ray regime of the spectra ([Torres 2018](#)). The value is chosen based on average best-fit values obtained from previous studies.

Fig. 1 shows examples of our spectral fits for some new pulsars presented in the 3PC. The model is able to reproduce the spectra of the whole population of gamma-ray pulsars. Thanks to its flexibility, it can resemble the wide variety of gamma-ray spectra, from those with very narrow peaks to those with broader peaks, looking almost flat at energies of ~ 1 GeV. Regarding pulsars with X-ray data, results are very similar to [Íñiguez-Pascual et al. \(2022a\)](#): the gamma-ray range is reproduced in all the cases, and the X-ray band is well matched in the majority of them with a single set of parameters.

Values of the best-fit parameters are similar to those obtained in previous works. Small values of lengthscale x_0 are obtained, and reinforce the idea that a relevant synchrotron contribution is required to explain the zoo of observed gamma-ray spectra. Again, young and millisecond pulsars are equally well fitted. The only difference between these two groups is the preference of millisecond pulsars for larger values of the parallel electric field $E_{||}$ (and lower values of the lengthscale x_0), as we have already observed in previous works ([Viganò et al. 2015b](#); [Torres et al. 2019](#)). For each pulsar, the best-fit values of the spectral parameters ($E_{||}$, b , x_0) and the normalization N_0 are used in the geometrical model to generate light curves, whose fitting is presented in the next section.

3.3 Searching for correlations between spectral parameters

[Viganò et al. \(2015b\)](#) showed the existence of some trends between spectral and physical parameters of pulsars. Now that the number of observed gamma-ray pulsars has increased, it is a good exercise to check whether the found correlations remain or not, and if new ones appear. To appoint something as a significant correlation we follow the same criterion as in [Viganò et al. \(2015b\)](#) and require a Pearson r value larger than 0.85. We only consider spectral parameters that have been correctly determined, i.e. those of pulsars whose spectra data fulfills the quality criterion stated in subsection 3.1.

The most relevant correlation found is indeed between the spectral parameters $E_{||}$ and x_0 , with parameters of the best-linear fit very similar to those of the previous study (see Section 5 of [Viganò et al. \(2015b\)](#) for a discussion on the physical implications of this correlation). The correlation between $E_{||}$ and the magnetic field strength at the light cylinder B_{lc} and that of N_0 and the theoretical gamma-ray luminosity L_{theo} are now still statistically significant but do not reach our Pearson r threshold, probably due to the enlargement

of the population. In both cases the parameters of the best linear-fit are very similar to the previous ones. The other correlations presented in that paper involved parameters of the phenomenological function PLEC1 ([Abdo et al. 2012](#)) from the 2PC, which has been updated to the PLEC4 ([Abdollahi et al. 2022](#)) on the 3PC. No correlations of the PLEC4 model parameters with our (spectral or geometrical) model parameters are found.

4 FITTING OBSERVATIONAL LIGHT CURVES

4.1 Important considerations prior to fitting

Fitting synthetic light curves to observational ones is not a straightforward task and several considerations have to be taken into account before addressing it.

Fermi gamma-ray light curves in the 3PC differ in the number of phase bins with which they are described. For each particular pulsar we then adapt the construction of the theoretical emission maps depending on its number of phase bins. For pulsars with 25, 50 or 100 observational phase bins, we fix the number of synthetic azimuthal bins to 25, 50 or 100, respectively. For pulsars with 200, 400 or 800 observational bins, we set the number of synthetic bins to 100, in order to keep the computational time affordable, since having more bins in the map requires to add more trajectories to the simulation to have an acceptable map resolution. We thus rebin the observational light curves with 200, 400 and 800 bins to have 100 bins in total. Notice that by doing this we are losing some information, but what we lose are small-scale features of the observational light curve that our model at its current stage is still not able to reproduce.

In addition, observational light curves have a certain level of background resulting from detected photons that do not come from the pulsar itself. In the 3PC, a background level is estimated for each pulsar, being computed from the photon weights and indicated in the pulse profile plots by a black dashed line. Our synthetic light curves do not have such background, because the theoretical emission maps represent all the emission coming from the pulsar, and only from the pulsar. Therefore we subtract to each observational light curve its corresponding background level obtained from the 3PC before comparing with synthetic predictions.

We shall impose a data quality criterion before fitting light curves, and do not consider light curves with only 25 observational bins. These have very large errors and their shape is generally not well defined yet. We also require that a spectral fit can be performed for the pulsars for which we fit the light curves, but here without imposing any restriction on the quality of their spectral data, since in [Íñiguez-Pascual et al. \(2024\)](#) we demonstrated the small impact of the spectral parameters on the shape of the light curves. The population available for our fitting contains 226 gamma-ray light curves after these quality cuts.

For each one of these 226 pulsars (with particular values of P , \dot{P} and spectral parameters) we generate 30 emission maps, evenly sampling ψ_Ω values from 3° to 90° (we avoid the case of an aligned rotator, $\psi_\Omega = 0^\circ$, because no pulsed emission would be seen), and consider 51 observers, θ_{obs} , evenly distributed between -90° and 90° .

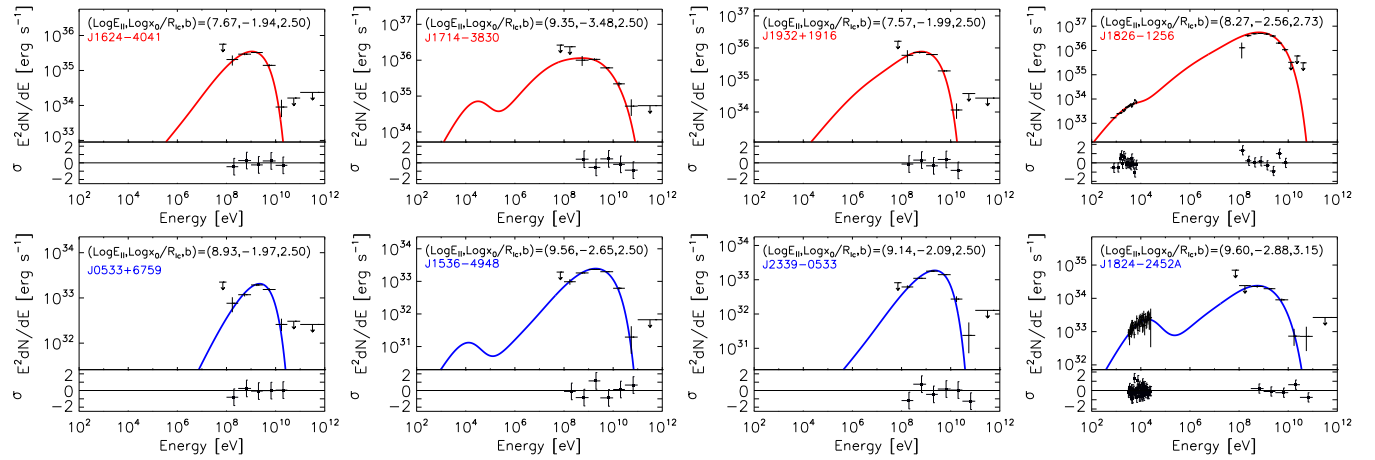


Figure 1. Examples of best-fitting spectra of some of the new pulsars reported in gamma-rays in the 3PC. Red (blue) lines are used for young (millisecond) pulsars.

4.2 Fitting procedures

We compare the whole synthetic sample of light curves we have generated for each particular pulsar with the corresponding observational light curve. Below, we present and discuss different metrics used here to do such a comparison.

4.2.1 Fitting procedure in the time domain

The reduced χ^2 method can be used similarly to what is done in the spectral fitting, here to assess the goodness of the fit of I_i^{obs} by I_i^{syn} , i.e. the intensities (in weighted counts/bin units) of the observational and synthetic light curves, respectively. In our synthetic light curves, phase $\phi_\Omega = 0$ corresponds to the plane containing the rotational and magnetic axes, but this is arbitrary. For this reason, synthetic and observational light curves are not necessarily aligned. In order to find the best alignment, we rotate each synthetic light curve and compute the reduced χ^2 value for all rotations (as many as the number of observational bins), keeping the smallest one as the reduced χ^2 of that synthetic light curves set. We reverse each synthetic light curve to obtain an additional one available for fitting. Two pulsars with the same geometrical parameters but spinning in opposite directions would a priori create different light curves. However, since an inversion in the direction of rotation of the star is equivalent to a pulsar turned upside down and our region possesses an equatorial symmetry, in our model one light curve would be the reversed version of the other. In addition, we normalize the synthetic light curves to the observational ones by using the standard, analytical linear regression formula: a normalization factor N_{lc} is found by solving $\partial\chi^2/\partial N_{lc} = 0$ and multiplied to our synthetic light curves.

However, fitting light curves with χ^2 has some intrinsic caveats (see [García & Torres \(2025\)](#) for a deeper discussion). For example, a small phase variation of one peak in multi-peaked light curves results in a large χ^2 value, even though the two light curves compared are visually very similar. Fig. 2 shows two examples of cases in which χ^2 selects a best fit for which the peak structure is not well reproduced, and therefore it is not convincing from a human eye perspective.

In addition, in light curves with narrow peaks, χ^2 can be

biased towards synthetic light curves reproducing the observational bins with emission close to the background but failing to reproduce the peaks: since all bins contribute with equal weights to χ^2 , a good adjust to many low-flux bins could give an overall small value for χ^2 even when the peaks are not matched at all. In order to reduce this effect, an approach similar to the one proposed in [Churazov et al. \(1996\)](#) can be taken and consider a weighted reduced χ^2 (we shall keep calling it χ^2 for simplicity), in which each bin's squared difference is weighted by the normalized flux of the observational light curve, \bar{I}_i^{obs} , in order to give more weight to the bins with higher flux, as

$$\bar{\chi}_w^2 = \frac{1}{n-2} \sum_i \frac{(I_i^{obs} - I_i^{syn})^2 \bar{I}_i^{obs}}{(\delta I_i^{obs})^2}, \quad (1)$$

where n is the number of bins of a light curve in time domain, the 2 value represents the number of free parameters in the fitting, I_i^{obs} and I_i^{syn} are the intensities of the observational and synthetic light curves, respectively, and δI_i^{obs} is the observational error. In this way, more weight is given to the peaks, and we are promoting to properly reproduce the peaks rather than the low-flux level parts of the light curves. Middle panels of Fig. 2 present the best-fitting light curves found with the weighted χ^2 showing that the caveats associated to the normal χ^2 no longer appear. Notice that the weighted χ^2 is also not a perfect metric: the peak tails of the chosen best-fit synthetic light curves deviate more from the observational ones than in the regular χ^2 case. Hereafter, we will use Eq. 1 for the light curve fitting, keeping in mind in any case the unavoidable freedom in choosing a given metric for the comparison, and how the choice is driven by the above mentioned visual, subjective considerations about when a fit is satisfactory or not.

4.2.2 Fitting procedure in the frequency domain

In parallel, we apply a Fast Fourier Transform (FFT) to all light curves existing in time domain to bring them into frequency domain, \hat{I}_k^{obs} and \hat{I}_k^{syn} , whose amplitude is

$$\|\hat{I}_k\| = K \left\| \sum_{j=0}^{n-1} I_j e^{-i2\pi k j/n} \right\|, \quad (2)$$

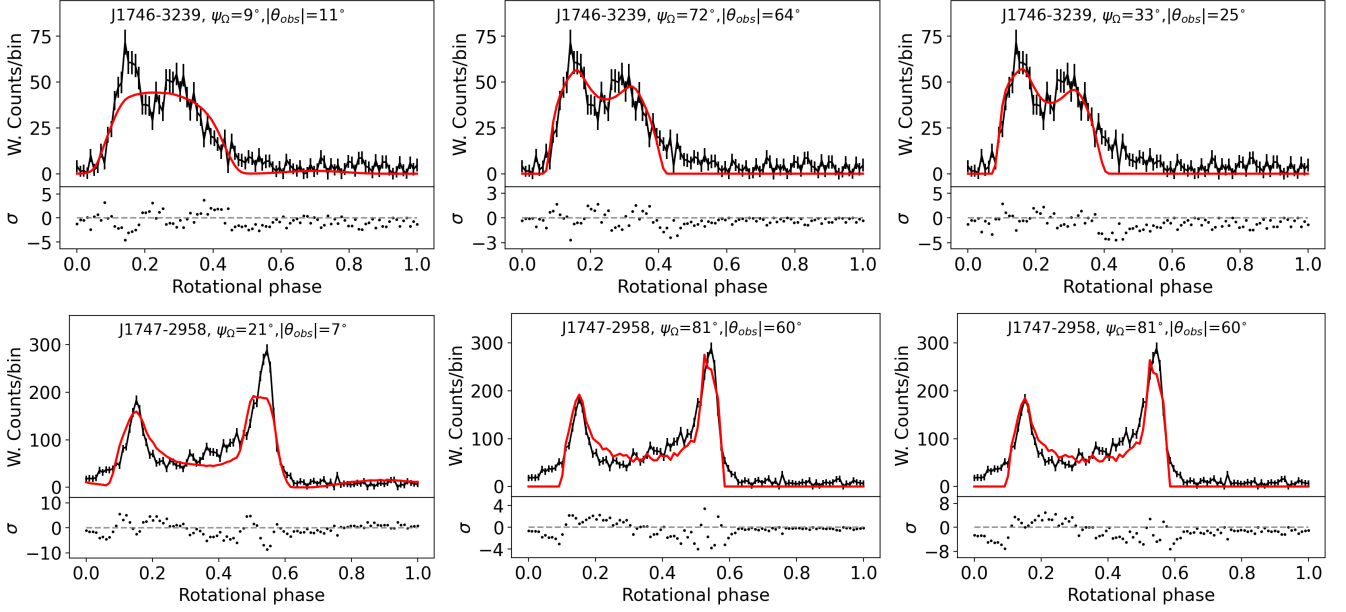


Figure 2. Examples of the caveats intrinsically associated with a fitting with χ^2 and possible solutions, for the pulsars J1746 (top row) and J1747-2958 (bottom row). From left to right: best-fitting light curve with a normal χ^2 , best-fitting light curve with a weighted χ^2 and best-fitting light curve recovered with the inverse transform from fitting in the frequency domain.

where K is a normalization factor. We normalize the amplitude of the observational Fourier transform to its maximum. Each synthetic transform is normalized to match the peak value of the observational one, which is usually at $k = 1$ or 2 , with few cases being at 3 or 4 . k is the harmonic, which goes from 1 to $n/2$ (we neglect $k = 0$, the average flux of the light curve). Harmonics are the sub-signals forming the complete light curve in time domain, having $k+1$ nodes. The amplitude of the Fourier transform of a light curve with a single peak roughly symmetric in the rise and decay, will be dominated by odd harmonics, while that of a light curve with a double (roughly symmetric in rise and decay) peak, with a 0.5 phase separation, will be dominated by even harmonics. Different phase separations, the presence of sub-structures and asymmetries in the rise and decay features can redistribute the amplitude to the harmonics with the opposite parity. The width of the peak(s), and the relative peak flux between two peaks, will also determine how the amplitude is distributed over the harmonics. In order to assess the impact of the higher harmonics in the fit, we have tried to filter out the Fourier transforms by only considering the harmonics lower than a given maximum harmonic $k_{max} = 5, 10$ or 15 . Even with the extreme case of $k_{max} = 5$, in several cases the shape of the best-fitting light curve barely differs from the complete best-fitting transform. Larger values of k_{max} leaves untouched a growing number of best-fit solutions, and for k_{max} the differences are negligible. Fig. 3 shows a couple of examples. This points out the negligible effect of the higher harmonics in the FFT fitting, which is mostly defined by the lowest harmonics.

We compare the amplitudes² of the observational and syn-

thetic Fourier transforms, $\|\hat{f}_k^{obs}\|$ and $\|\hat{f}_k^{syn}\|$, respectively, with a simple euclidean distance (ED) as comparative metric,

$$ED = \sqrt{\sum_k \left(\|\hat{f}_k^{obs}\| - \|\hat{f}_k^{syn}\| \right)^2}. \quad (3)$$

Comparing light curves in frequency domain focuses more on the symmetries and overall structures of the light curves. Moreover, it has computational benefits, since it's phase invariant. The cost of the Fourier transform is less than the cost of ranging all the possible phase alignments and inversion of the curve in the time domain. See Appendix B for further computational costs considerations.

4.2.3 Fitting using dynamic time warping

García & Torres (2025) has recently introduced the Dynamic Time Warping (DTW) as a method to assess the similarity between light curves, which we could in principle use for our light curve fitting. DTW compares the sequence of data points between two time series without requiring alignment in phase Berndt & Clifford (1994). As a result, it is flexible to local stretching or compression in time, allowing it to recognize structural resemblance between light curves regardless of the values of the phases associated with each point. Therefore, a good fit can be assigned to e.g. light curves having similar overall structures of peaks and sub-peaks, but very different peak widths, or phase separations between peaks. Furthermore, its computational requirements, lasting five orders of magnitude more of time than the fitting in frequency domain and three times more than the fitting in time domain (see Appendix B), makes its usage for light curve fitting still not agile enough. Therefore, DTW application for light curve fitting, although promising, with the current implementation is not practically feasible.

² Considering the amplitude instead of the power (which is equal to the squared amplitude) is arbitrary. We have performed tests using the power of the Fourier transforms in the fitting and very similar results are obtained.

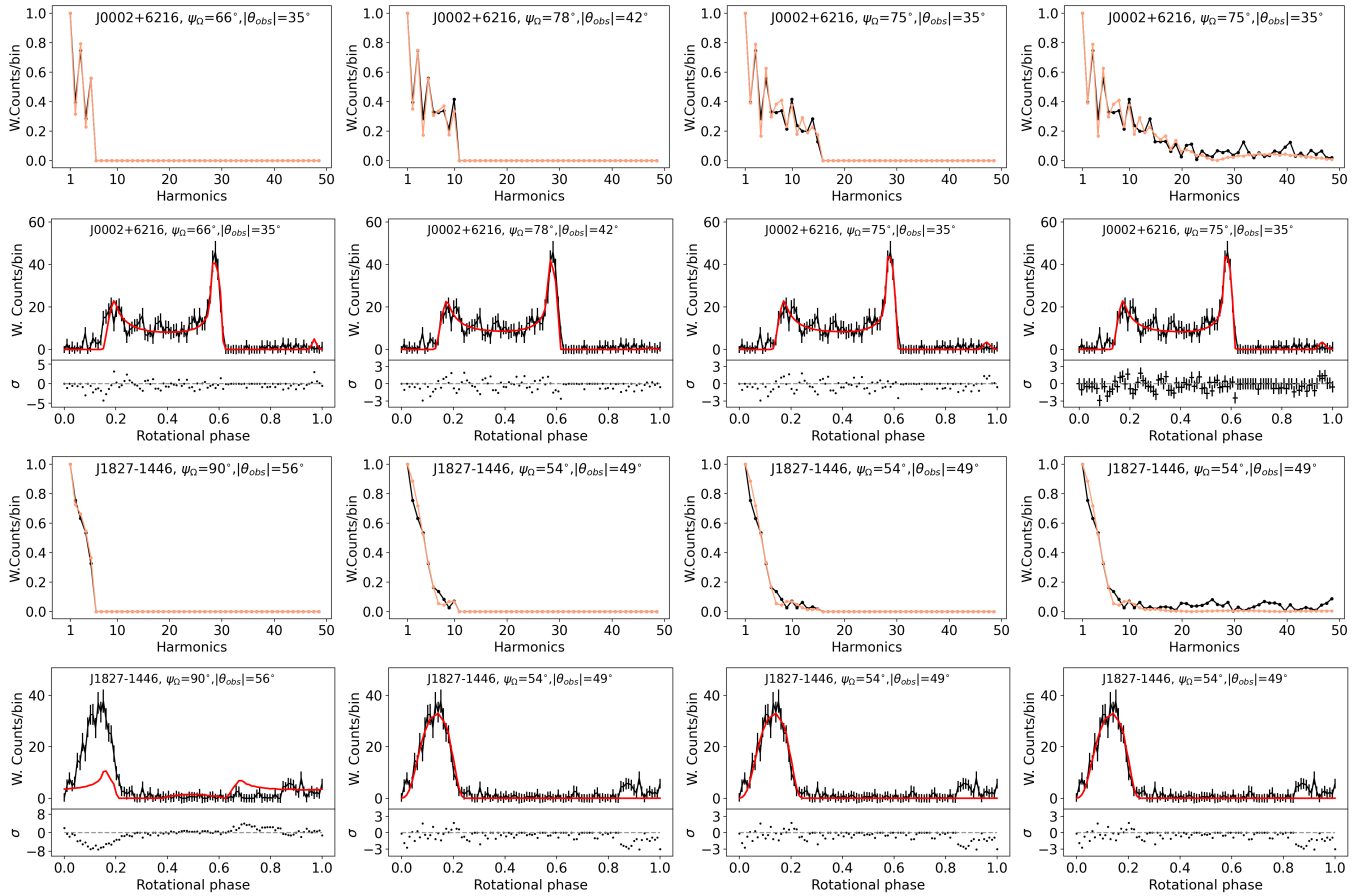


Figure 3. Examples of best-fitting light curves in frequency domain for different values of k_{max} for two pulsars, J0002 +6216 on first (Fourier transforms) and second (recovered light curve in time domain) rows and J1827-1446 on third (Fourier transforms) and fourth (recovered light curve in time domain) rows. In all rows, from left to right: $k_{max} = 5$, $k_{max} = 10$, $k_{max} = 15$ and case without filtering.

5 RESULTS

Figure 4 shows examples of best-fitting light curves resulting from both temporal and frequency techniques, for some selected pulsars. All fits for those pulsars with at least 50 observational phase bins in their light curves are shown in Appendix C, Figure C1. Table C1 shows the best-fit values of the geometrical parameters for all the pulsars fitted. In general, we note that results of the fits obtained with χ^2 in time domain and with ED in frequency domain are qualitatively similar.

In many cases the best-fitting synthetic light curves visually resembles well the observational one, with some remarkable fits, such as those of J1044-5737, J1112-6103, J1600-3053, J1641-5317, J1811-2405, J1906+0722, J1907+0602 or J2111+4606. Note the diversity of light curve shapes that we can reproduce, for both young and millisecond pulsars. In most of the cases we are able to catch the overall structure of the observational light curves, reproducing number of peaks and their widths, separation of peaks, and even peak flux ratio in some cases. In several cases we also reproduce the so-called bridge emission, which, in our model, comes from the outermost parts of the trajectories, which are more curled.

However, our model is not able to capture the small scale features of the light curves of some pulsars, as J0002+6216 or J1713+0747. Another aspect in which the model struggles to

reproduce is when very asymmetric peaks are present, as in J0218+4232. In other cases, like J1124-5916 and other with high-quality data (i.e. small errors), we are not able to reproduce specific flux ratios and/or cusped peaks. With only two free geometrical parameters at play, our emission region does not have the complexity that the real magnetosphere surely possess, meaning that we cannot generate light curves as complex as those observed for some pulsars. In a few cases, such as J1536-4948 or J1630+3734, the model is not providing a good fit.

Looking at the performance of both fitting techniques, we note that both of them find good fits in a number of cases and fail in others. In about a fifth of the sample, both methods give compatible best-fit parameters (within one step in the sweeping grid of values of each parameter).

Figure 4 also presents the contour plots of χ^2 and ED for each pulsar, showing the values of these statistics in the space of parameters $\theta_{obs}-\psi_{\Omega}$. Due to the equatorial symmetry in the skymaps, we only show θ_{obs} from 0° to 90° . In many pulsars, the contours from both techniques are not identical but show different regions of low χ^2 and ED. This underscores the distinct performance and intrinsic focus of both methods. The most relevant features of these plots are in fact the valleys present in many cases, both in the χ^2 and the ED ones, pointing out a degeneracy in the geometrical parameters. Along the valley of parameter degeneracy, good fitting

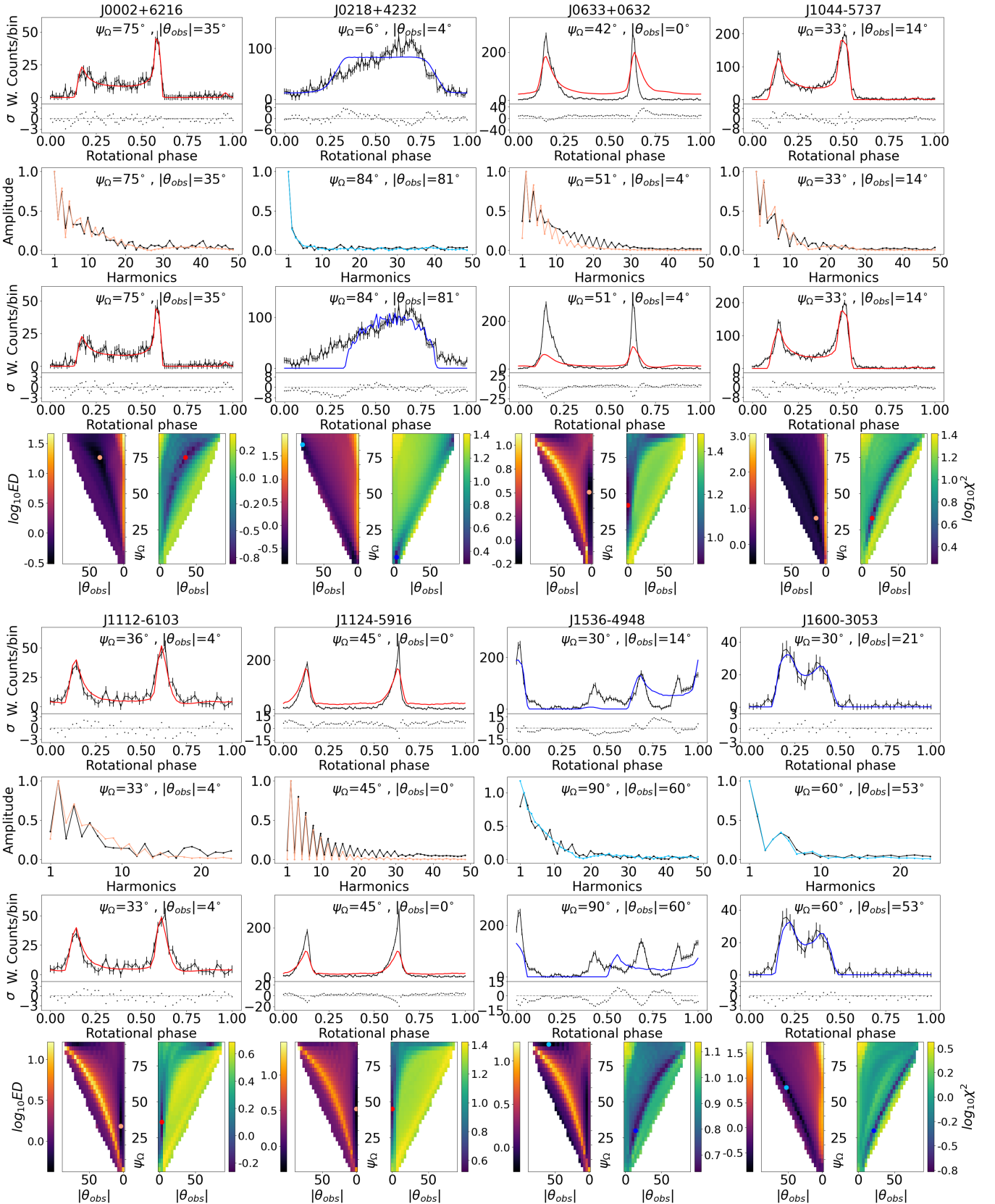
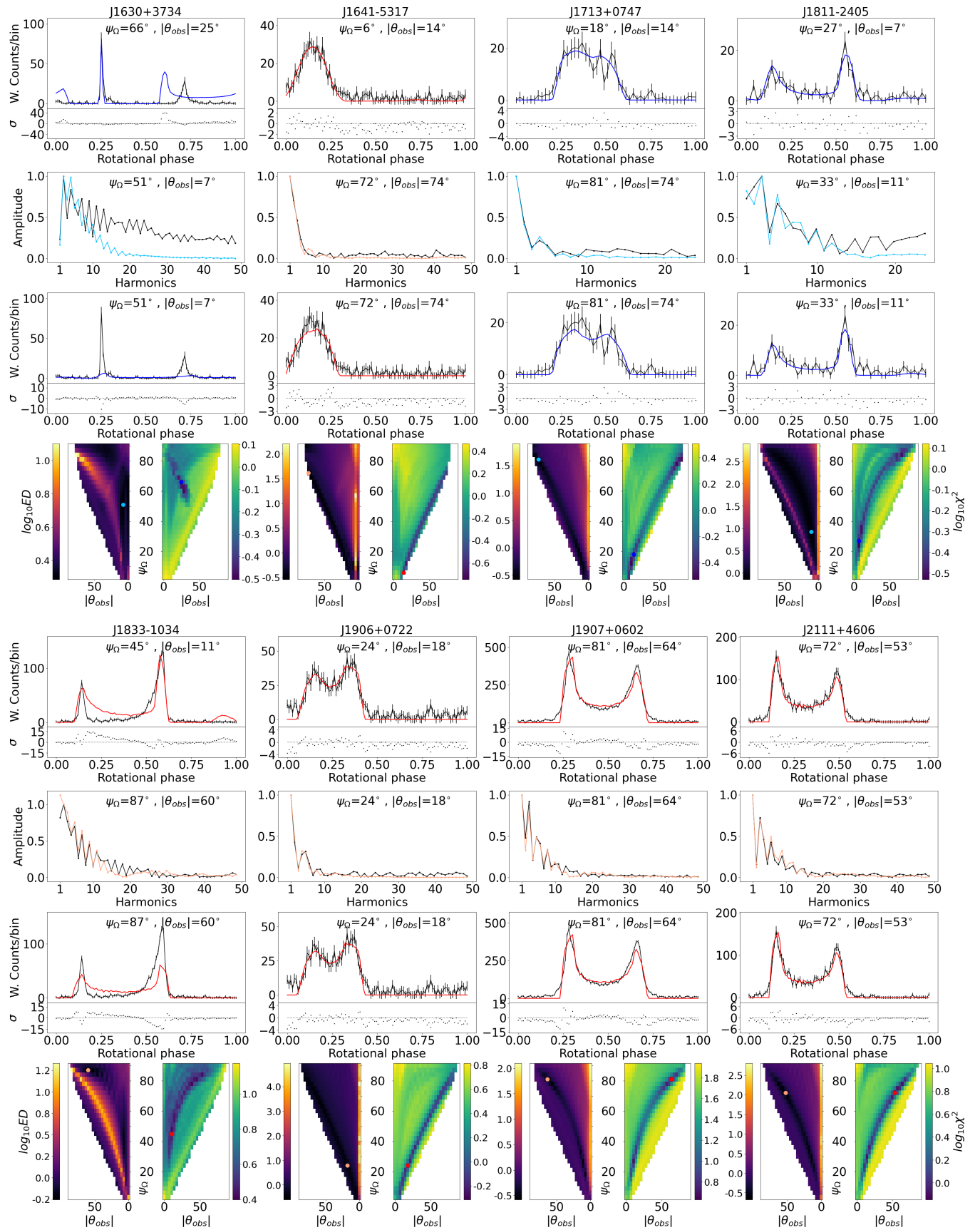


Figure 4. Best-fit light curves obtained in time and frequency domain for two sets (four rows each) of four pulsars (one per column). The first and fifth rows correspond to fits in the time domain. Second and sixth rows show the best-fit Fourier transform in the frequency domain fits, and third and seventh the light curve recovered with the inverse transform (with the best alignment in phase and spin direction (see Section 4.2.1)). The fourth and eighth rows show the contour plots of both χ^2 in time domain and ED in frequency domain. Dots correspond to best-fit geometries from the fitting in time domain (dark colors) and from the fitting in frequency domain (light colors). Red (blue) lines correspond to synthetic light curves of young (millisecond) pulsars, and black lines to observational lightcurves.

Figure 4. - *continued*

geometrical values can be found in almost the whole range of θ_{obs} or ψ_{Ω} , as can be seen in the χ^2 contour plot of J1747-2958 in Fig. 5. In this figure we also show some other light curves whose set of parameters lie in the valley, apart from the best-fitting one under the χ^2 methodology. We see that the shapes of the not-best-fitting light curves (fuchsia and green dots) are rather similar, even though their geometrical parameters are very different. Models with more asymmetry in the shape of the emitting region would likely break this degeneracy.

We have investigated how the results we found are affected by the grid resolution of the geometrical parameters by performing fits of several pulsars with a thinner grid, considering 90 values of ψ_{Ω} and 151 values of θ_{obs} , i.e. increasing the resolution a factor 3. The results were not significantly changed. The best fit light curves chosen were the same or with best-fit parameters close to those of the best-fit light curves with the default resolution, and the contour plots were basically the same. In particular, neither new substructures appeared in the contour, nor it helps breaking the degeneracy.

5.1 Fitting all light curves with a single set of maps

In [Íñiguez-Pascual et al. \(2024\)](#) we stated the idea that, in our model, the spectral and timing properties barely affect the set of light curves, which are controlled basically by the two geometrical parameters. In other words, the emission map (and the set of associated light curve) are insensitive to the spectra that fits a specific pulsar. This implies that a set of synthetic light curves produced for a fixed set of best-fit spectral parameters but varying the geometry (inclination, observer line of sight) is also representative of the global set of all observed pulsars, for which the values of such angles are also randomly distributed. We can explore this further asking whether it is possible to fit the whole population of observational light curves with just a set of emission maps in which timing and spectral parameters are fixed to those of an arbitrary pulsar. To answer this question, we have fitted the whole sample of light curves generated for a randomly-selected young pulsar, J1838-0537, to the whole set of observational light curves in the same way as explained before. We find that the fitting results are qualitatively very similar to those of the fitting in which each observational light curve is compared to the synthetic light curves generated for its corresponding pulsar. The same conclusions we have presented in this section in terms of quality of the fits are also found now, independently of which fitting method is used. Considering χ^2 in time domain, the distribution of the statistics values of the normal fitting and the one using a single set of skymaps is almost identical, as shown in Figure 6. This exercise has been repeated using the maps from a millisecond pulsar, J1035-6720, and the exact same results are obtained. These results, again, back the statement that geometry is the defining aspect for the light curves shapes; and that the global structure of the magnetosphere as well as the emission processes and location of the accelerating region must be roughly the same, regardless of different timing properties, spectra. We stress that this might not be the case if also X-ray light curves were to be taken into account, since a strong link between X- γ spectral differences and X- γ light curve differences is expected, since the synchrotron radiation is spread to a broader angles. Our result is in agreement with the recent observational proof

by [García & Torres \(2025\)](#). These authors quantified 3PC light curve similarity and showed it can be very high for very different pulsars; even some MSPs and young pulsars share detailed light curve morphology.

5.2 Searching for correlations between geometrical parameters

The geometrical parameters show no correlation with any other parameter of the pulsar or the model, and all pairs have a Pearson coefficient r smaller than our threshold of 0.85, i.e. there is no significant correlation of the geometry with spectral parameters, timing quantities, or PLECA parameters. The former reinforces the idea that there is a decoupling between spectral and geometrical parameters, backing a conclusion obtained in [Íñiguez-Pascual et al. \(2024\)](#): spectral and timing considerations are negligible in shaping gamma-ray light curves, being geometrical ones much more relevant. This conclusion may, of course, be affected by adding further complexities in our model.

6 CONCLUSIONS

In this paper we have presented the first concurrent fitting of spectra and light curves for the whole population of gamma-ray pulsars. Using an effective radiative model based on synchro-curvature radiation and the computation of the dynamics and emission of charged particles in a pulsar's magnetosphere, we generate synthetic spectra. Intertwined with the spectral calculation, we describe the geometry of the trajectory of these particles and define a particular shape for the region where they move, which allows us to produce light curves. Theoretical spectra and light curves are then compared with observational spectral and light curves data to assess the ability of our models to reproduce them and to find the best-fitting values of the free model parameters, three in the spectral model and two in the geometrical model.

The spectral model fits well the whole population of gamma-ray spectra, obtaining similar results to previous systematic fittings carried out by the authors. For the first time we have fitted the individual gamma-ray light curves. We have made use of two different techniques: using the reduced χ^2 (weighted with the normalized flux of the observational light curve) to evaluate the goodness of the fits of light curves in time domain, and computing the euclidean distance to compare the light curves in frequency domain, i.e. to compare their Fourier transforms. Despite the caveats that both methods may have, the two of them give qualitatively similar results. With both fitting methods we have obtained good fits in many cases. For most pulsars we capture the general structures of the observational light curves, such as number of peaks and separation between peaks, or even flux ratio between peaks or width of the peaks, but fail to reproduce the small scale features. In a few pulsars, the observational light curves are not found in our set, either because they simply don't exist or because the fitting techniques miss them. Regarding the first possibility, the effective nature of the geometrical model provides versatility at an acceptable computational cost, but it is still lacking the complexity that a real magnetosphere may have. The model does not generate very complex synthetic light curves, for example with

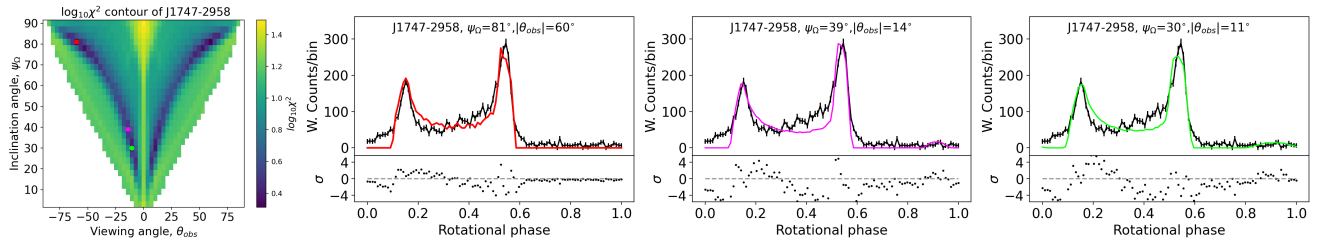


Figure 5. Examples of the degeneracy in the contour plots. Left panel shows the χ^2 contour plot of J1747-2958 with dots corresponding to the light curves depicted on the other three panels. From left to right: χ^2 best-fitting light curve in red, and other light curves with geometries on the χ^2 valley, in fuchsia and green.

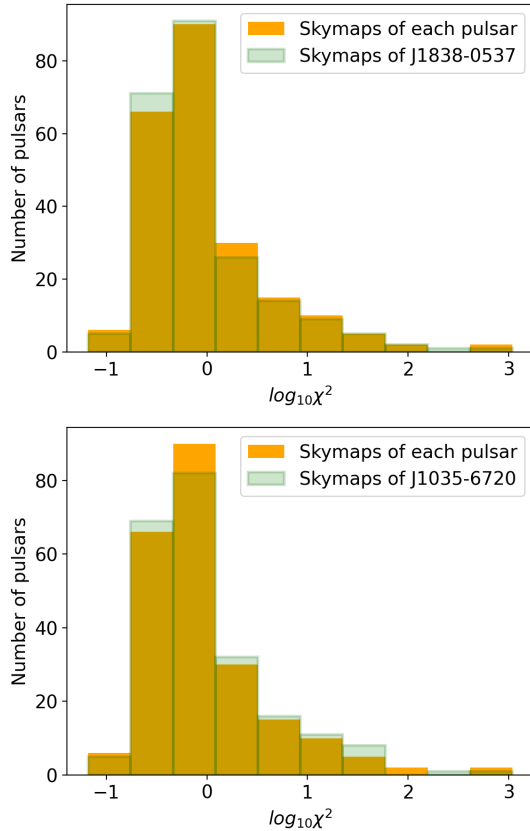


Figure 6. Comparison of χ^2 distributions of all fits obtained with each pulsars' skymaps (orange histograms) and considering only one set of skymaps for all pulsars (green histograms). The green histogram in the top (bottom) panel corresponds to the fitting done with the skymaps of J1838-0537 (J1035-6720).

very asymmetric peaks or containing significant substructures (e.g. small peaks near larger ones). An improvement of the model, making it more realistic but maintaining the effective approach and the computational cost acceptable, is planned for the future.

We have found the distributions of best-fit viewing angles for both fitting methods to differ from a uniform distribution, as it should be a priori, showing an overabundance of small viewing angles. We argue that the reason is the way we model the light curves and the assumptions we make, as well as the fact that we are considering the fits from all pulsars together, without taking their goodness into account.

We have also done the exercise of fitting the whole population of gamma-ray light curves with just a single sample of emission maps, generated for a specific a set of P , \dot{P} and spectral parameters. Overall results of this fitting are very similar to those obtained in the fitting in which each observational light curve is fitted with its corresponding sample of skymaps. This seems to point towards a unique magnetospheric structure of pulsars' magnetosphere and a unique process generating the radiation, with pulsars' detected emission being solely defined by the inclination angle of the pulsar and the viewing angle of the observer. We also have to admit the possibility that the assumptions in our model, in particular the effective weight to enhance the small parts of the trajectories which give synchrotron-dominated emission, might lead to this effect, by construction. Future improvement of the underlying physics of the model, which will allow to convert effective parameters into more physical ones, will shed more light into this.

At this point is relevant to comment on the only fitting of 3PC gamma-ray light curves done so far, very recently published in Cerutti et al. (2024), in order to contextualize our work in the present panorama of modeling of pulsar high-energy emission. The results presented there and in the present work are qualitatively similar but are based on different assumptions and approaches. Both can fit well some light curves and capture the global structure of most of the cases, but fail when fitting complex light curves (with asymmetric peaks or small scale features). While we use an effective model, austere, and with low computational cost, Cerutti et al. (2024) develop magnetospheric PIC simulations in which the electromagnetic fields and charged particles are self-consistently computed and are computationally very costly. The qualitative similarity of the results obtained with such different (and complementary) models provides support for the current general understanding of the generation of the pulsar high-energy emission.

Finally, we have studied the possible correlations between pulsar parameters in the same way we did in Viganò et al. (2015b). The relevant correlation between the $E_{||}$ and x_0 is significantly found again, but there is no significant correlation between the PLEC4 model parameters from the 3PC and our model parameters. No correlation of the geometrical parameters with any other parameter or physical quantity is found.

ACKNOWLEDGEMENTS

We thank C. R. García for the useful discussions. This work has been supported by the grant PID2021-124581OB-I00 funded by MCIU/AEI/10.13039/501100011033 and 2021SGR00426 of the Generalitat de Catalunya. This work was also supported by the Spanish program Unidad de Excelencia María de Maeztu CEX2020-001058-M and by MCIU with funding from European Union NextGeneration EU (PRTR-C17.I1). DIP has been supported by the FPI predoctoral fellowship PRE2021-100290 from the Spanish Ministerio de Ciencia, Innovación y Universidades and his work has been carried out within the framework of the doctoral program in Physics of the Universitat Autònoma de Barcelona. DV is funded by the European Research Council (ERC) under the European Union's Horizon 2020 research and innovation programme (ERC Starting Grant IMAGINE, No. 948582).

DATA AVAILABILITY

In the text we cite the sources of the data we use in our study, no new observational data is herein presented. Any additional theoretical detail required is available from the authors upon reasonable request.

REFERENCES

- Abdo A. A., et al., 2012, *ApJ*, **744**, 146
 Abdo A. A., et al., 2013, *The Astrophysical Journal Supplement Series*, **208**, 17
 Abdollahi S., et al., 2022, *ApJS*, **260**, 53
 Bai X.-N., Spitkovsky A., 2010, *ApJ*, **715**, 1270
 Benli O., Pétri J., Mitra D., 2021, *A&A*, **647**, A101
 Berndt D. J., Clifford J., 1994, in KDD Workshop. <https://api.semanticscholar.org/CorpusID:929893>
 Cao G., Yang X., 2019, *ApJ*, **874**, 166
 Cerutti B., Philippov A. A., Spitkovsky A., 2016, *MNRAS*, **457**, 2401
 Cerutti B., Figueiredo E., Dubus G., 2024, *arXiv e-prints*, p. [arXiv:2412.02307](https://arxiv.org/abs/2412.02307)
 Chang S., Zhang L., Li X., Jiang Z., 2019, *MNRAS*, **488**, 4288
 Cheng K. S., Zhang J. L., 1996, *ApJ*, **463**, 271
 Churazov E., Gilfanov M., Forman W., Jones C., 1996, *ApJ*, **471**, 673
 Coti Zelati F., Torres D. F., Li J., Viganò D., 2020, *MNRAS*, **492**, 1025
 García C. R., Torres D. F., 2025, Quantitative exploration of the similarity of gamma-ray pulsar light curves ([arXiv:2503.02750](https://arxiv.org/abs/2503.02750)), <https://arxiv.org/abs/2503.02750>
 Íñiguez-Pascual D., Viganò D., Torres D. F., 2022a, *MNRAS*, **516**, 2475
 Íñiguez-Pascual D., Torres D. F., Viganò D., 2022b, *ApJ*, **933**, 234
 Íñiguez-Pascual D., Torres D. F., Viganò D., 2024, *MNRAS*, **530**, 1550
 Kalapotharakos C., Harding A. K., Kazanas D., 2014, *ApJ*, **793**, 97
 Kalapotharakos C., Brambilla G., Timokhin A., Harding A. K., Kazanas D., 2018, *ApJ*, **857**, 44
 Kalapotharakos C., Wadiasingh Z., Harding A. K., Kazanas D., 2023, *ApJ*, **954**, 204
 Pétri J., 2019, *MNRAS*, **484**, 5669
 Pétri J., Mitra D., 2021, *A&A*, **654**, A106
 Philippov A., Kramer M., 2022, *ARA&A*, **60**, 495

- Philippov A. A., Spitkovsky A., 2018, *The Astrophysical Journal*, **855**, 94
 Pierbattista M., Harding A. K., Grenier I. A., Johnson T. J., Caraveo P. A., Kerr M., Gonthier P. L., 2015, *A&A*, **575**, A3
 Romani R. W., Watters K. P., 2010, *ApJ*, **714**, 810
 Smith D. A., et al., 2023, *ApJ*, **958**, 191
 Torres D. F., 2018, *Nature Astronomy*, **2**, 247
 Torres D. F., Viganò D., Coti Zelati F., Li J., 2019, *MNRAS*, **489**, 5494
 Venter C., Harding A. K., Guillemot L., 2009, *ApJ*, **707**, 800
 Viganò D., Torres D. F., 2019, *MNRAS*, **490**, 1437
 Viganò D., Torres D. F., 2015, *MNRAS*, **449**, 3755–3765
 Viganò D., Torres D. F., Hirotani K., Pessah M. E., 2015a, *MNRAS*, **447**, 1164–1172
 Viganò D., Torres D. F., Martín J., 2015b, *MNRAS*, **453**, 2600–2622
 Watters K. P., Romani R. W., Weltevrede P., Johnston S., 2009, *ApJ*, **695**, 1289
 Yang X., Cao G., 2024, *ApJ*, **964**, 72

APPENDIX A: COMPARING OLD AND 3PC GAMMA-RAY DATA

As mentioned in the text, the spectral data presented in the 3PC for some pulsars differs from the data previously available (either in the 2PC or in dedicated studies), in shape but also in quality. In many cases one of the two sets of spectral data is clearly preferable than the other, for example because one of the two has more data points or smaller errors. The top row of Fig A1 shows the compared spectra of some pulsars in which the data previous to the 3PC (labeled for the sake of clarity as *Old*) is preferable to the given in the 3PC. In some cases it is not as clear, since both data sets have a very similar shape and quality. In these cases we take the data set with more continuous data points. Some examples are shown in middle row of Fig A1: for PSR J1600-3053, PSR J1959+2048, PSR J2017+0603 we choose the older data set and for PSR J1846+0919 the 3PC one. However, in some cases it is not possible to decide which set to choose, because shapes are very different (e.g. the spectra peaks at very different energies or have very different steepness at low energies). This occurs in 4 pulsars: J0248+6021, J0631+1036, J1023-5746 and J2030+4415. The bottom row of Fig. A1 shows these spectra.

APPENDIX B: COMPUTATIONAL COST OF THE LIGHT CURVE FITTING

The three light curve fitting techniques we have introduced in subsection 4.2 differ substantially in their computational requirements. For the three of them we use the same machine, the Ladon High-Performance Computing Cluster at the Institute of Space Sciences, ICE-CSIC. The fastest method is the euclidean distance in frequency domain, requiring ~ 0.37 minutes to fit the whole population of 226 pulsars. The weighted reduced χ^2 needs around two orders of magnitude more of time to complete the fitting, with ~ 25.42 minutes of computational time. Finally, DTW application to all pulsars (see its caveats as a fitting technique in the main text) would last $\sim 1.17 \times 10^4$ minutes, almost three orders of magnitude more than χ^2 in time domain and five more than ED in frequency domain. This huge computational requirement,

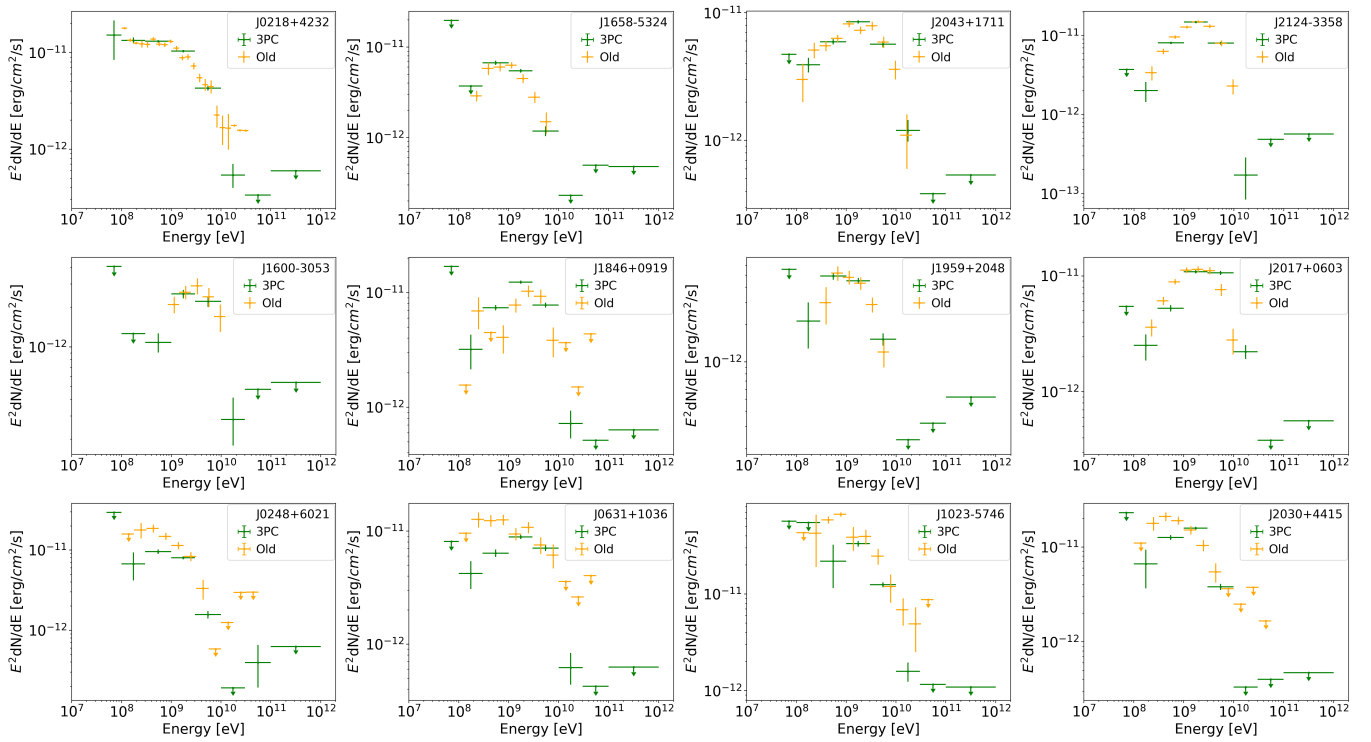


Figure A1. Comparison of spectral data from the 2PC or dedicated studies prior to the 3PC (in orange, labeled as *Old* for clarity) and from the 3PC (in green). The top row shows pulsars in which the old data is clearly better defining the spectra. In the middle row we show the pulsars in which there is a doubt about which data set is a better description. The bottom row shows pulsars for which both data sets are very different.

amounting more than eight days, even though is affordable, limits a lot the feasibility to carry on different tests, as we have done in this work.

APPENDIX C: LIGHT CURVE FITTING RESULTS

Figure C1 shows the plots of the best-fitting light curves in time and frequency domain, together with the contour plots of the statistics used in the fits, χ^2 and euclidean distance, respectively. Table C1 presents the best-fit geometrical values for all pulsars fitted.

Table C1. Best-fitting geometrical parameters (for fits in both time and frequency domain) of the pulsars on the 3PC.

Pulsar	Time domain		Frequency domain		Pulsar	Time domain		Frequency domain	
	$\psi_{\Omega} [^{\circ}]$	$ \theta_{obs} [^{\circ}]$	$\psi_{\Omega} [^{\circ}]$	$ \theta_{obs} [^{\circ}]$		$\psi_{\Omega} [^{\circ}]$	$ \theta_{obs} [^{\circ}]$	$\psi_{\Omega} [^{\circ}]$	$ \theta_{obs} [^{\circ}]$
J0002+6216	81	46	75	35	J1112-6103	30	4	33	4
J0007+7303	21	14	21	14	J1119-6127	9	11	30	25
J0023+0923	24	11	57	35	J1124-3653	66	35	87	53
J0030+0451	81	49	81	18	J1124-5916	48	0	45	0
J0034-0534	15	7	69	53	J1125-5825	81	49	66	32
J0101-6422	18	4	87	49	J1135-6055	9	7	78	74
J0102+4839	24	4	27	4	J1139-6247	27	21	27	21
J0106+4855	33	35	57	4	J1142+0119	84	74	72	60
J0205+6449	51	4	48	4	J1151-6108	81	53	87	39
J0218+4232	6	4	84	81	J1203-6242	36	4	39	4
J0248+4230	18	4	60	28	J1207-5050	3	4	57	0
J0251+2606	39	4	45	4	J1208-6238	42	4	42	4
J0307+7443	9	7	48	46	J1221-0633	72	71	45	42
J0312-0921	66	49	54	32	J1227-4853	6	4	42	32
J0318+0253	45	42	45	35	J1231-1411	81	53	72	21
J0340+4130	27	14	57	28	J1231-5113	36	0	30	0
J0357+3205	81	71	75	74	J1231-6511	3	11	78	67
J0359+5414	9	14	75	78	J1301+0833	87	78	87	71
J0418+6635	18	7	21	7	J1302-3258	90	71	81	71
J0437-4715	15	18	15	18	J1311-3430	18	7	69	42
J0514-4408	18	18	87	49	J1312+0051	21	11	45	46
J0533+6759	57	0	57	0	J1335-5656	45	35	54	42
J0554+3107	90	71	78	64	J1350-6225	42	0	54	0
J0605+3757	15	4	15	7	J1357-6429	3	7	81	81
J0610-2100	90	81	36	4	J1358-6025	21	11	78	67
J0613-0200	12	14	12	14	J1400-1431	78	78	78	78
J0614-3329	33	4	33	4	J1410-6132	12	0	90	74
J0621+2514	87	56	84	46	J1413-6205	69	46	69	42
J0622+3749	6	4	15	7	J1418-6058	87	56	24	4
J0631+0646	81	74	84	67	J1420-6048	24	14	72	60
J0633+0632	18	25	51	4	J1422-6138	24	14	21	11
J0633+1746	90	71	54	0	J1429-5911	33	4	27	4
J0659+1414	6	14	3	4	J1446-4701	63	56	54	35
J0729-1448	42	46	90	35	J1447-5757	3	4	81	78
J0734-1559	6	7	81	81	J1455-3330	60	42	57	35
J0740+6620	51	0	39	7	J1459-6053	6	7	6	7
J0742-2822	30	32	87	35	J1509-5850	15	11	78	71
J0744-2525	90	46	63	4	J1513-5908	3	0	57	53
J0751+1807	24	18	24	18	J1513-2550	45	11	60	28
J0802-5613	69	64	54	46	J1514-4946	75	53	72	49
J0835-4510	75	32	75	32	J1522-5735	18	4	15	4
J0908-4913	60	4	54	7	J1526-2744	9	18	12	4
J0931-1902	6	7	51	39	J1528-5838	9	11	81	78
J0940-5428	30	25	63	56	J1531-5610	6	11	90	78
J0952-0607	21	14	54	42	J1536-4948	18	7	90	60
J0955-6150	87	56	87	56	J1543-5149	78	78	42	35
J1012-4235	57	0	63	4	J1552+5437	90	81	90	78
J1016-5857	84	53	81	46	J1555-2908	48	7	84	32
J1019-5749	9	14	48	49	J1600-3053	30	21	60	53
J1024-0719	15	11	24	14	J1614-2230	90	67	63	4
J1028-5819	39	4	42	4	J1615-5137	27	18	69	64
J1035-6720	15	14	48	49	J1620-4927	12	7	81	74
J1036-8317	3	4	12	0	J1623-5005	75	56	75	56
J1044-5737	33	14	33	14	J1624-4041	27	4	30	4
J1048-5832	72	32	42	11	J1625-0021	21	11	3	4
J1048+2339	48	53	45	0	J1627+3219	54	46	51	42
J1055-6028	9	7	84	85	J1628-3205	87	71	87	67
J1057-5226	81	67	78	74	J1630+3734	39	39	51	7
J1057-5851	90	67	15	4	J1640+2224	54	39	51	32
J1105-6107	51	0	48	0	J1641+8049	33	4	84	32
J1105-6037	18	7	21	11	J1641-5317	6	14	72	74
J1111-6039	87	81	87	81	J1648-4611	21	14	75	67

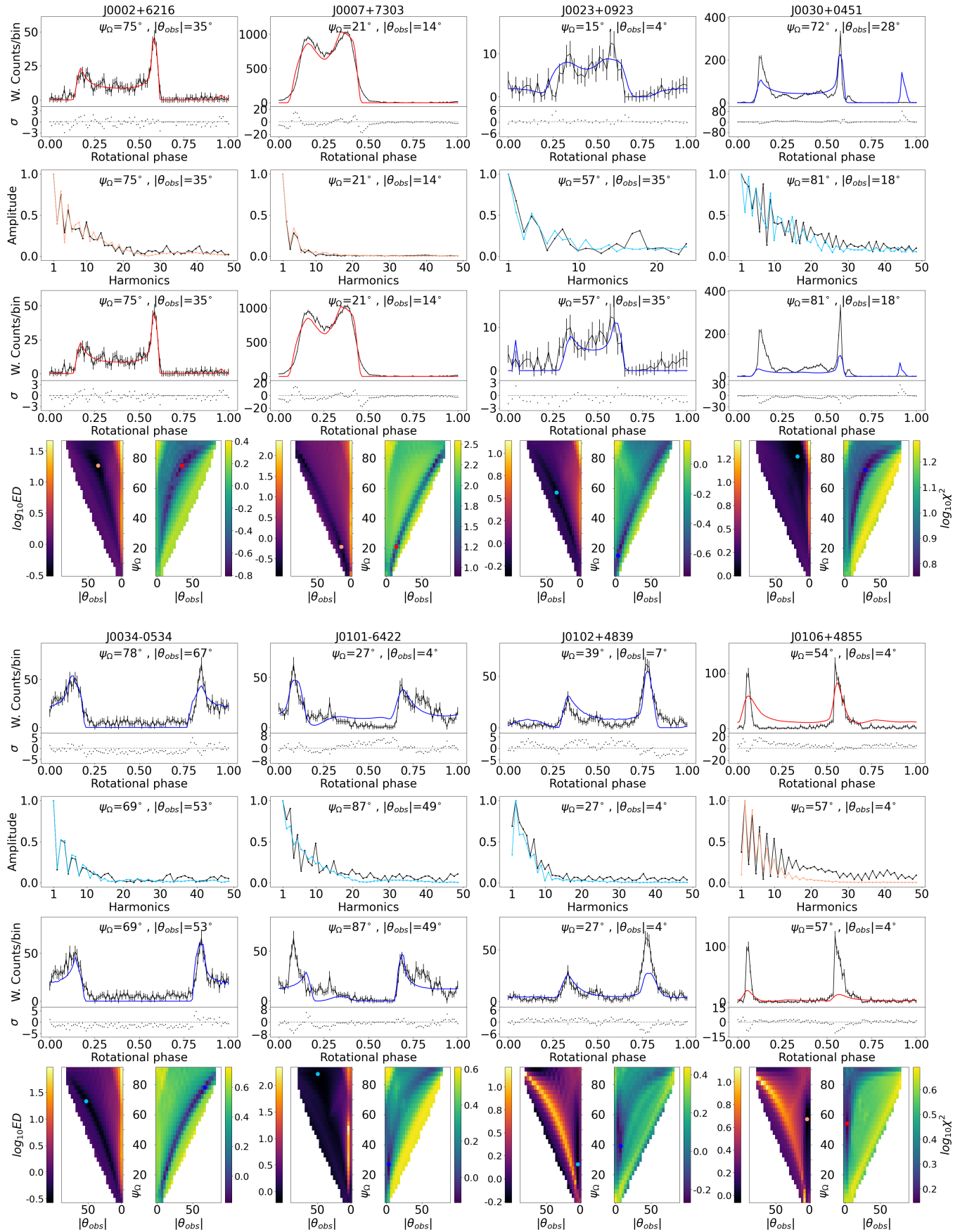


Figure C1. Best-fit light curves obtained in time and frequency domain. Panels and colors are as in Fig.4.

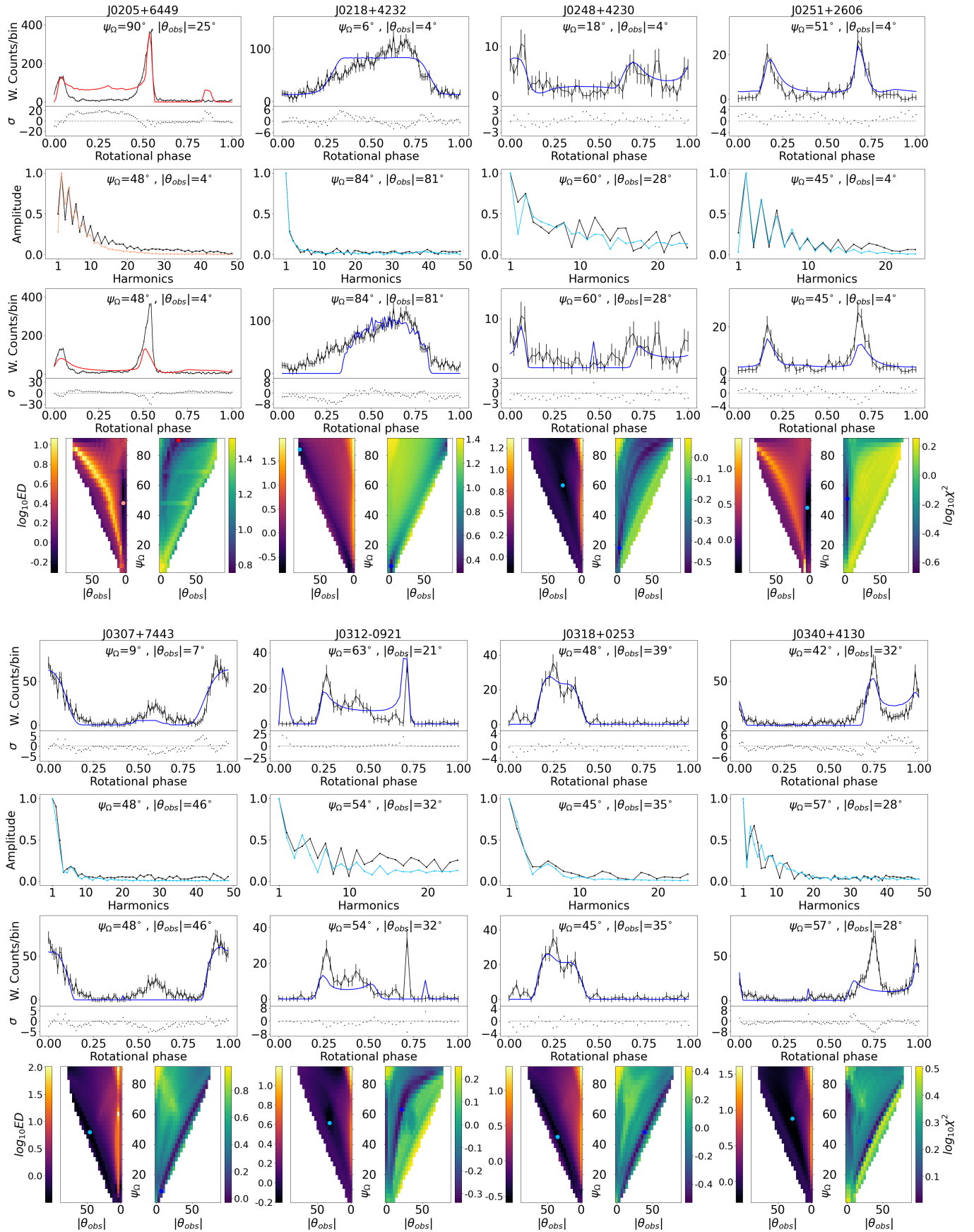


Figure C1. - continued

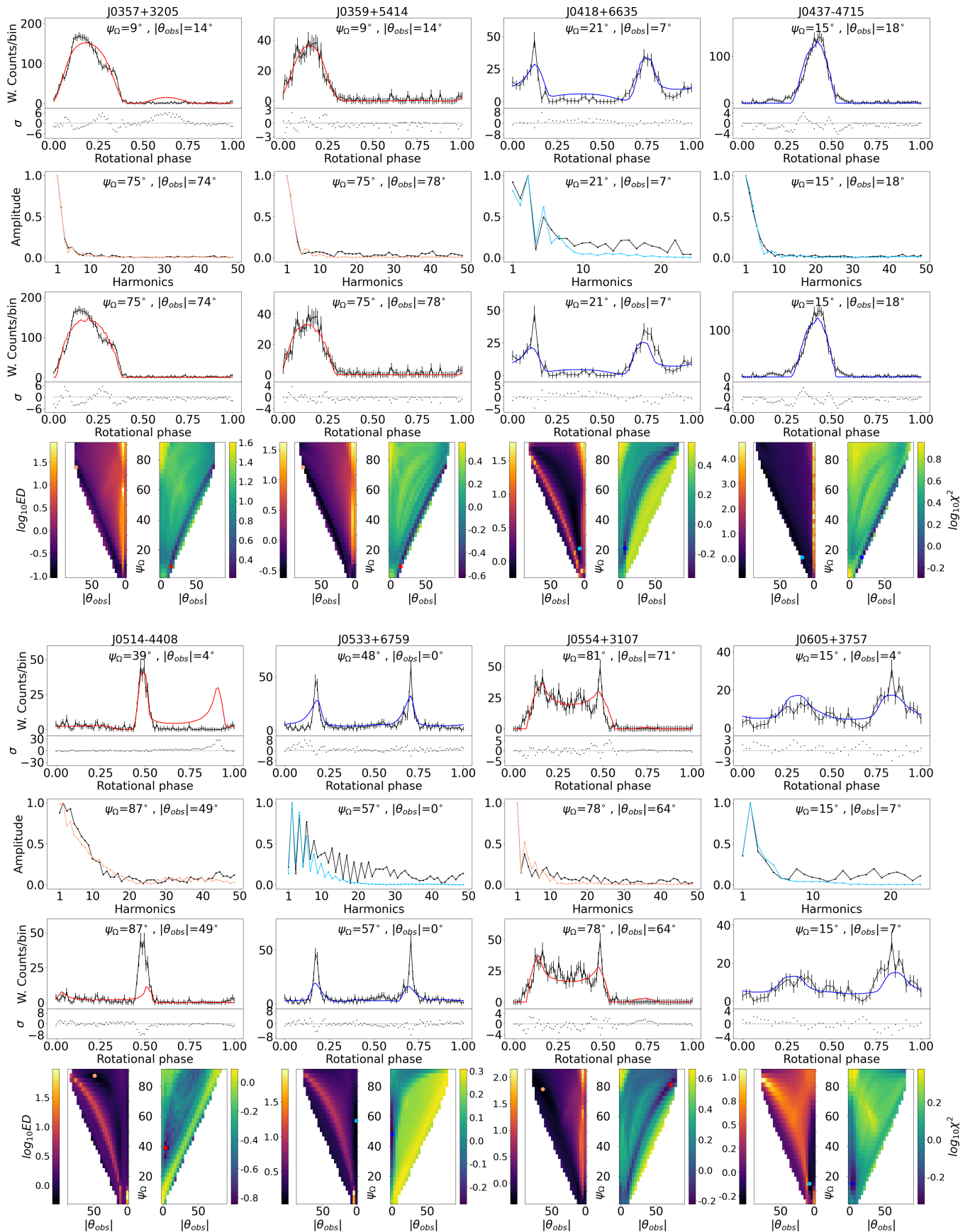


Figure C1. - continued

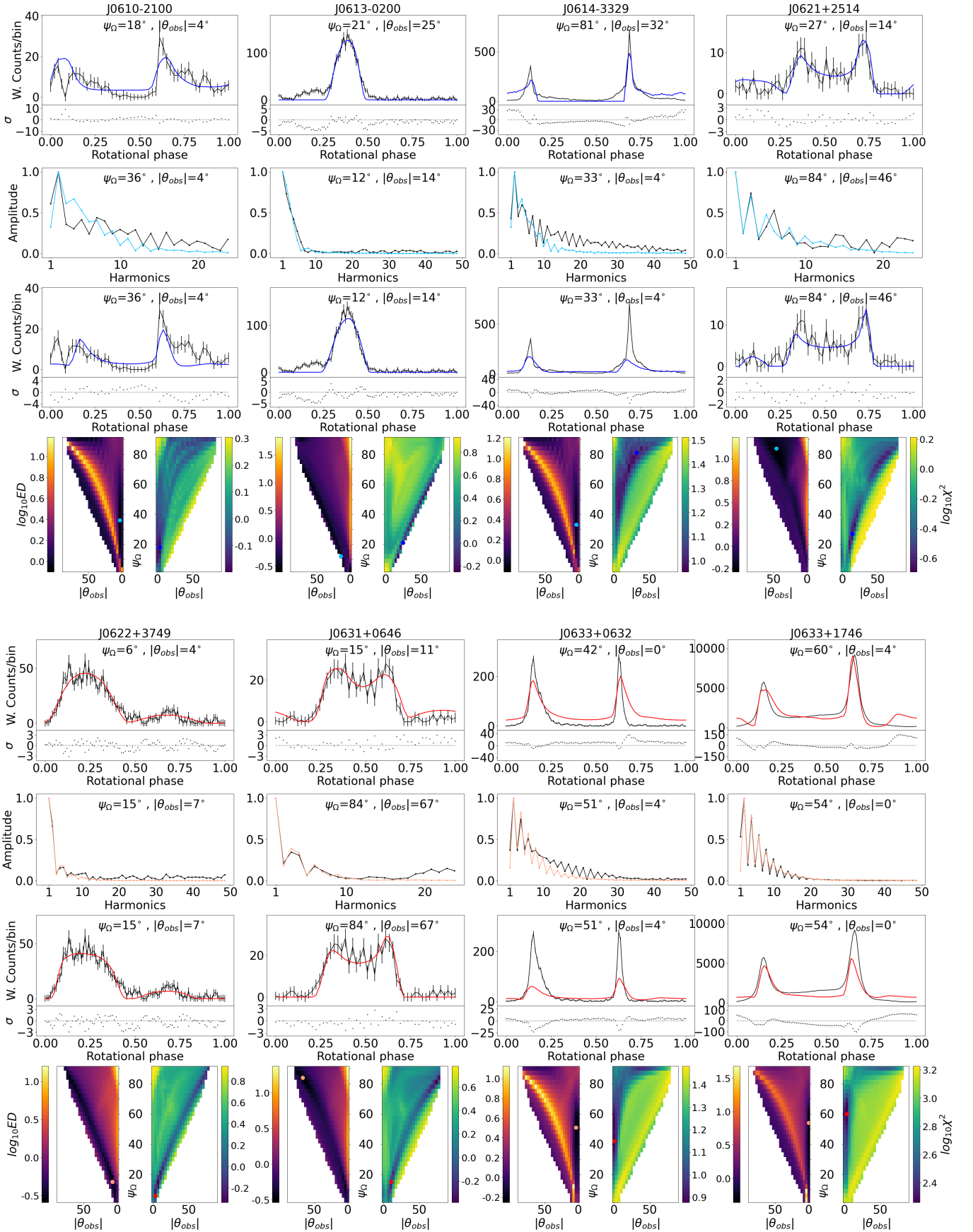


Figure C1. - continued

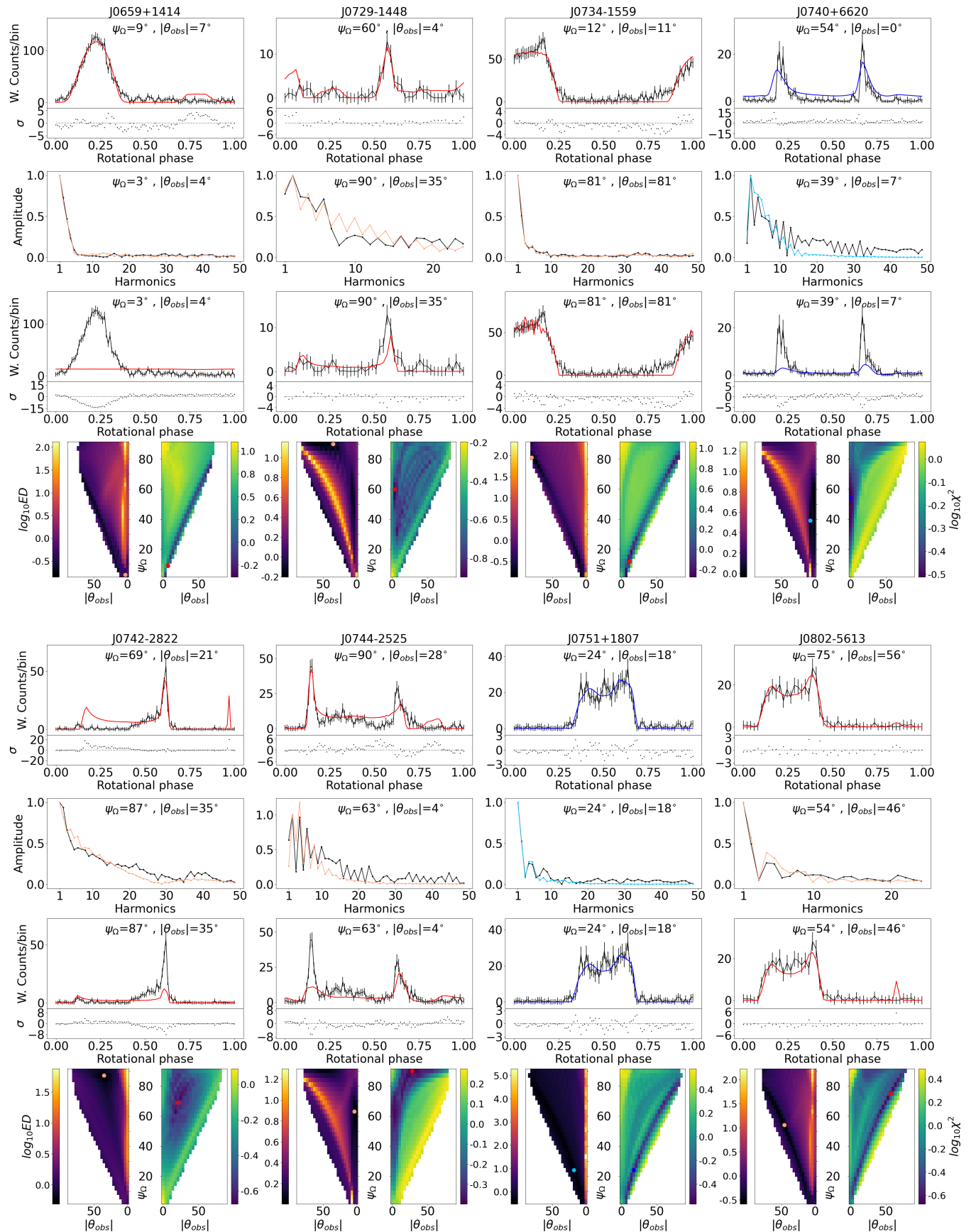


Figure C1. - continued

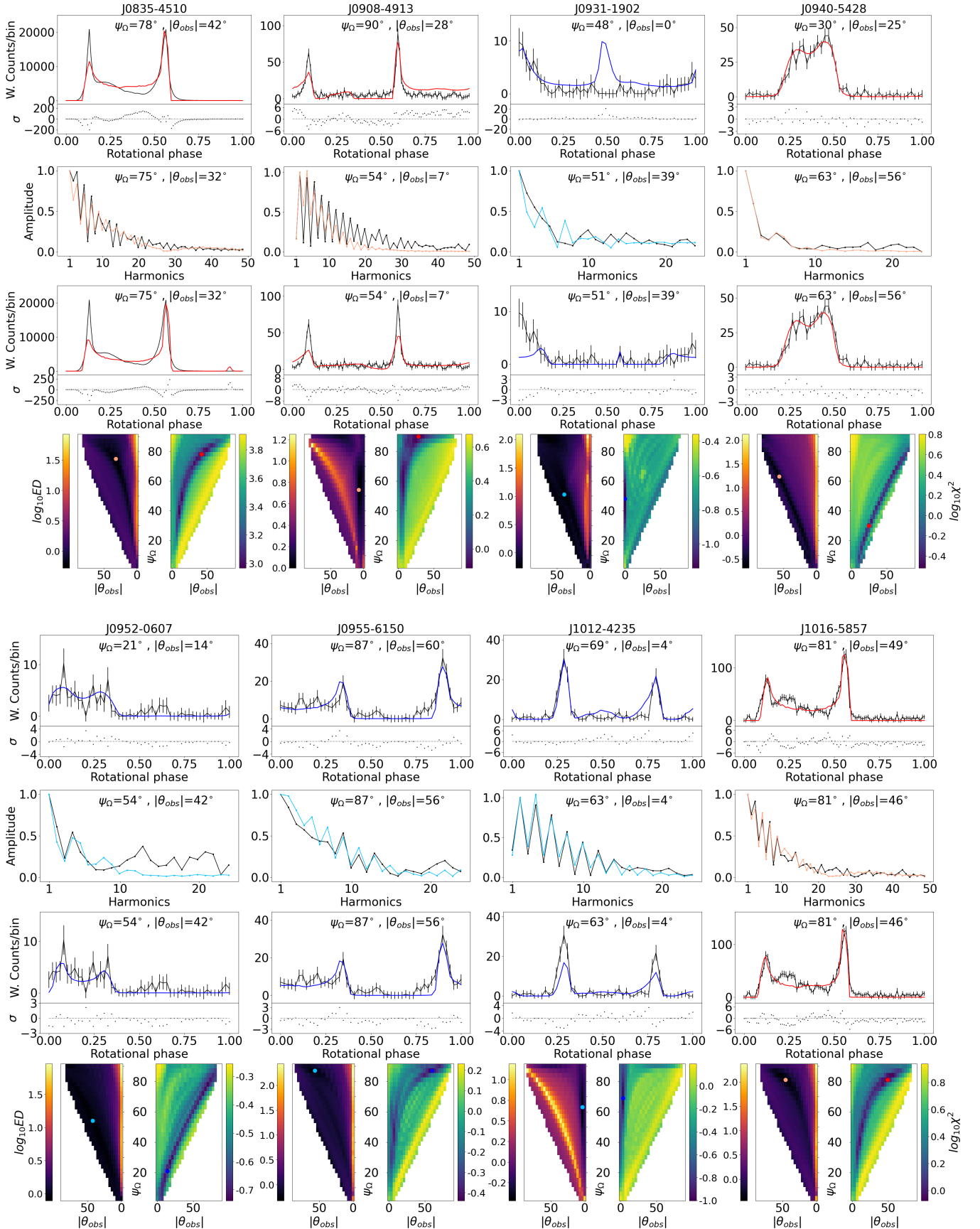


Figure C1. - continued

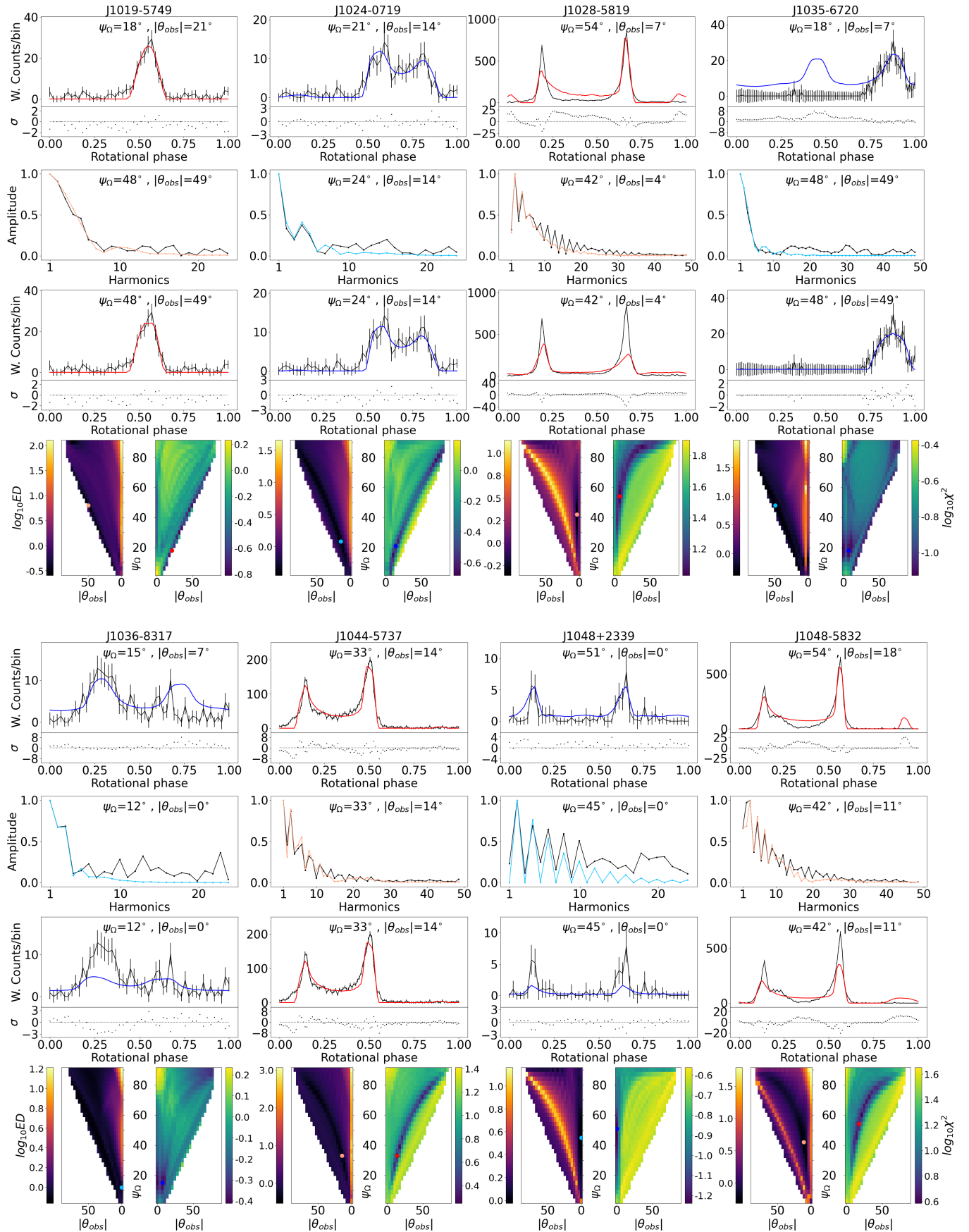


Figure C1. - continued

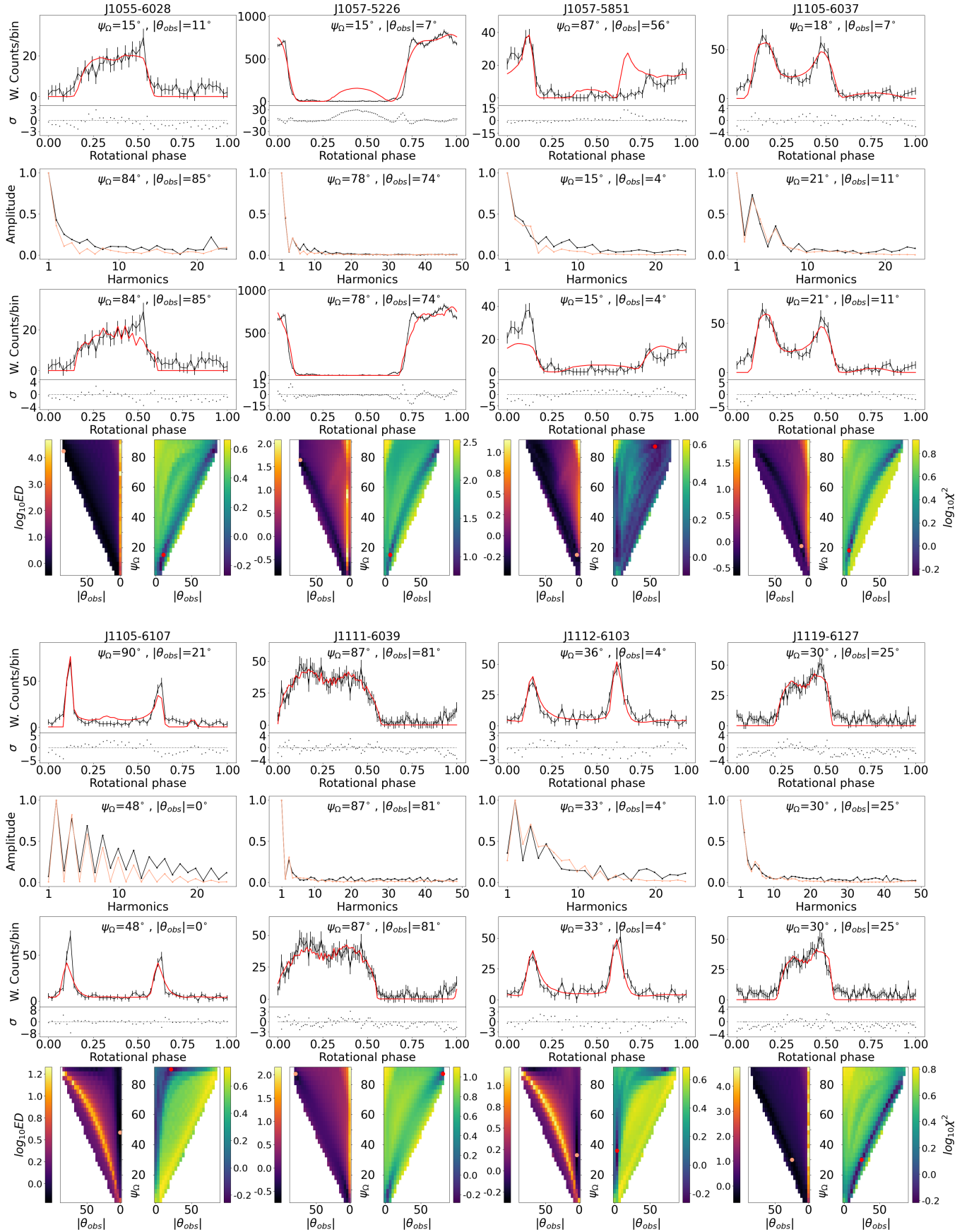


Figure C1. - continued

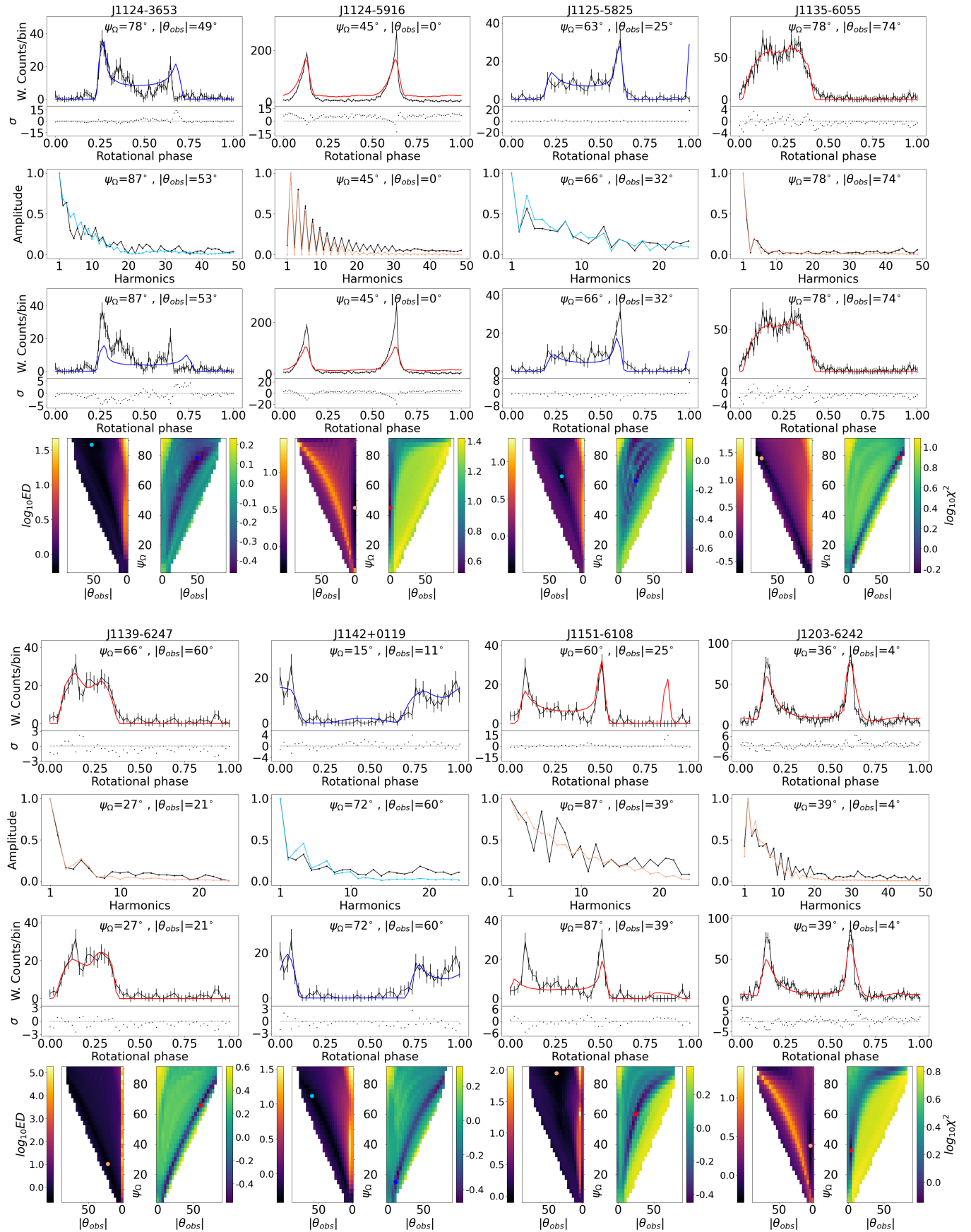


Figure C1. - continued

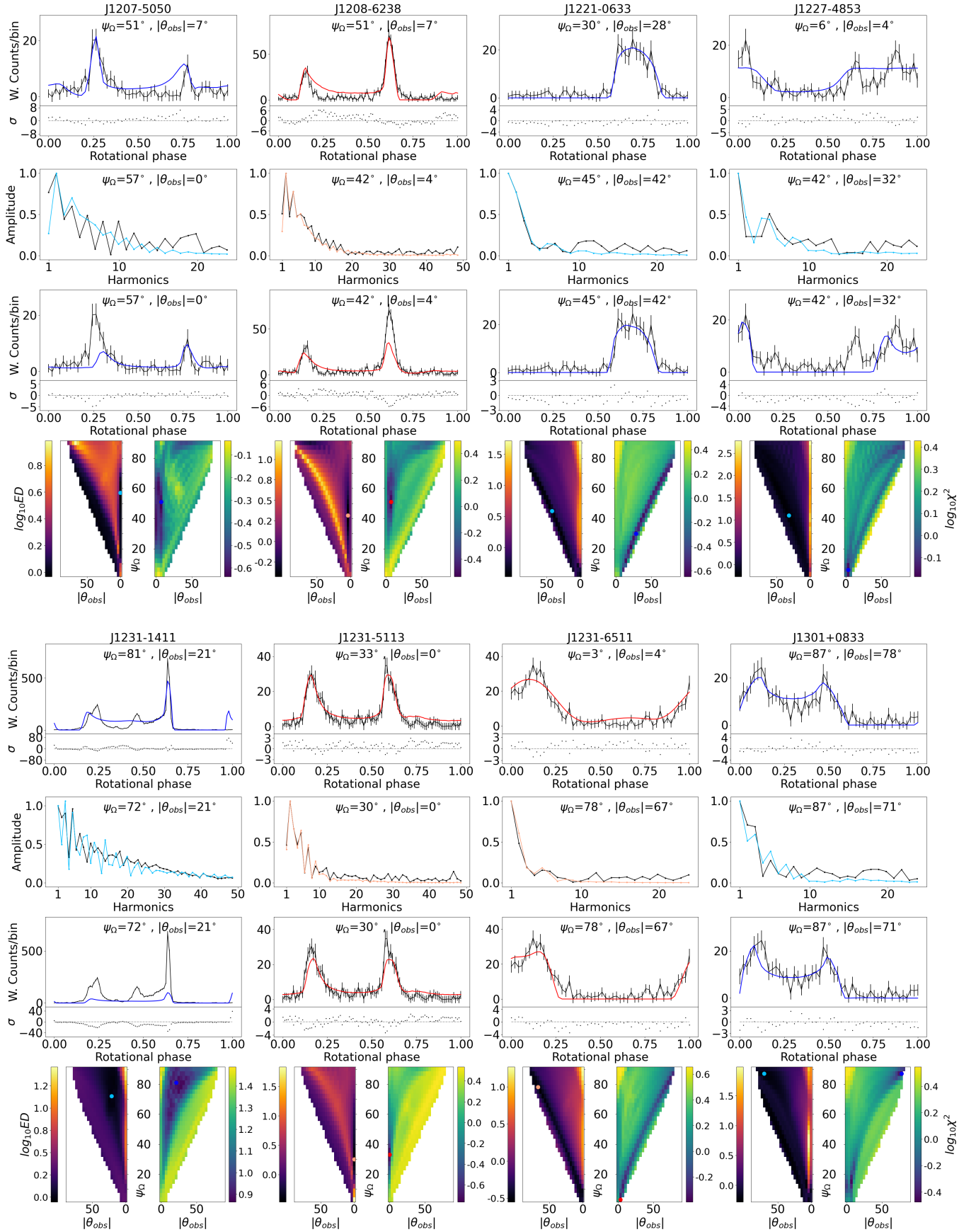


Figure C1. - continued

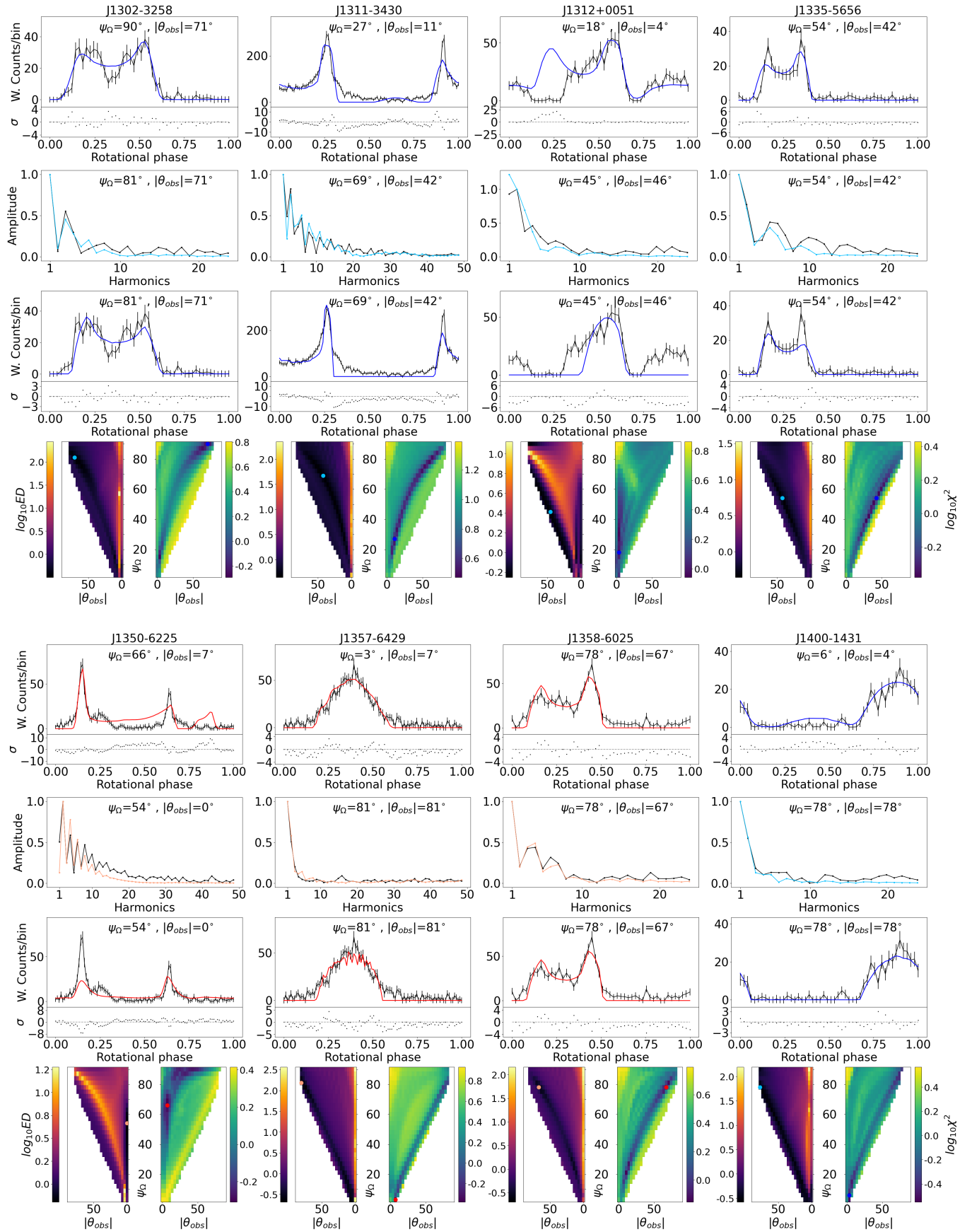


Figure C1. - continued

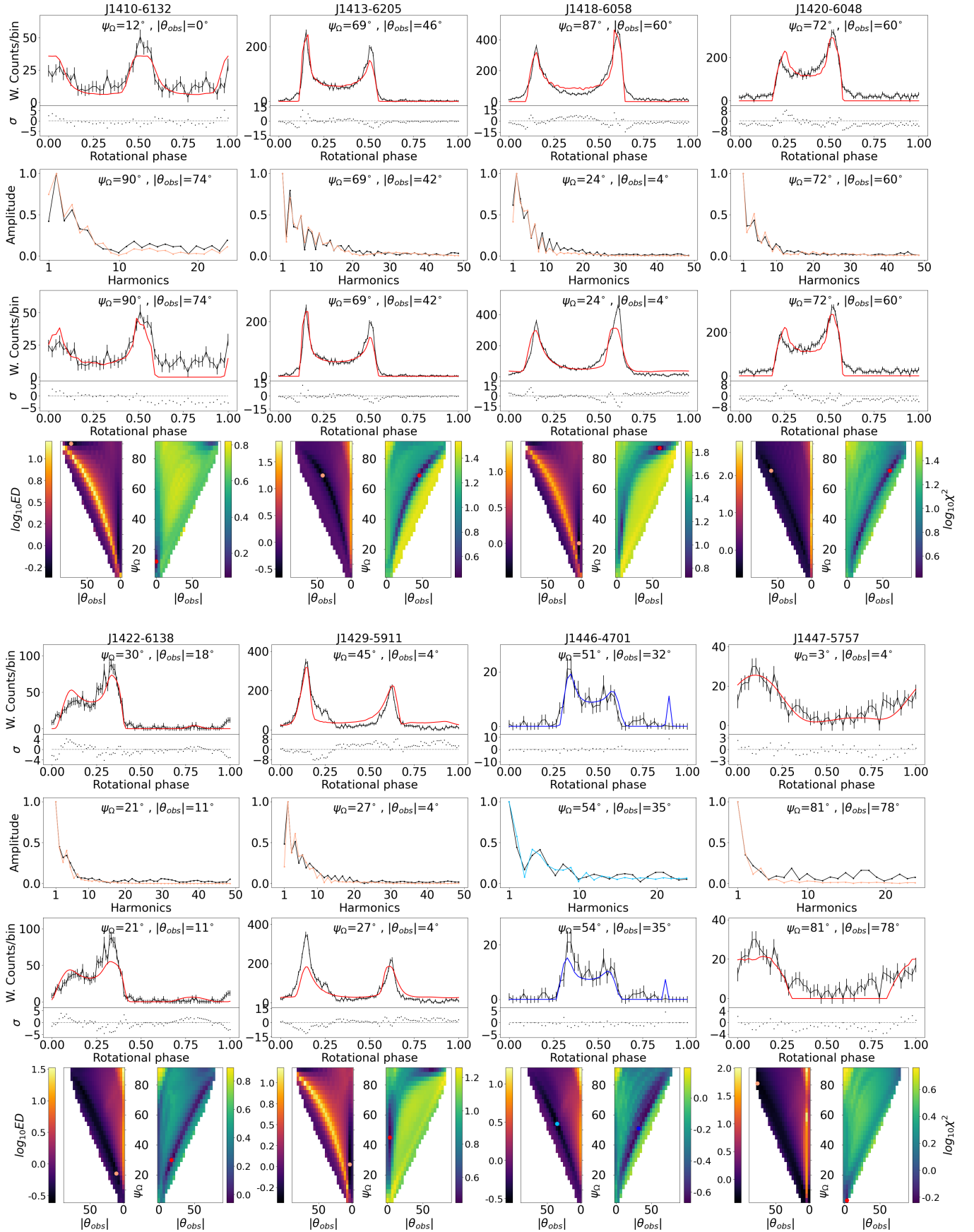


Figure C1. - continued

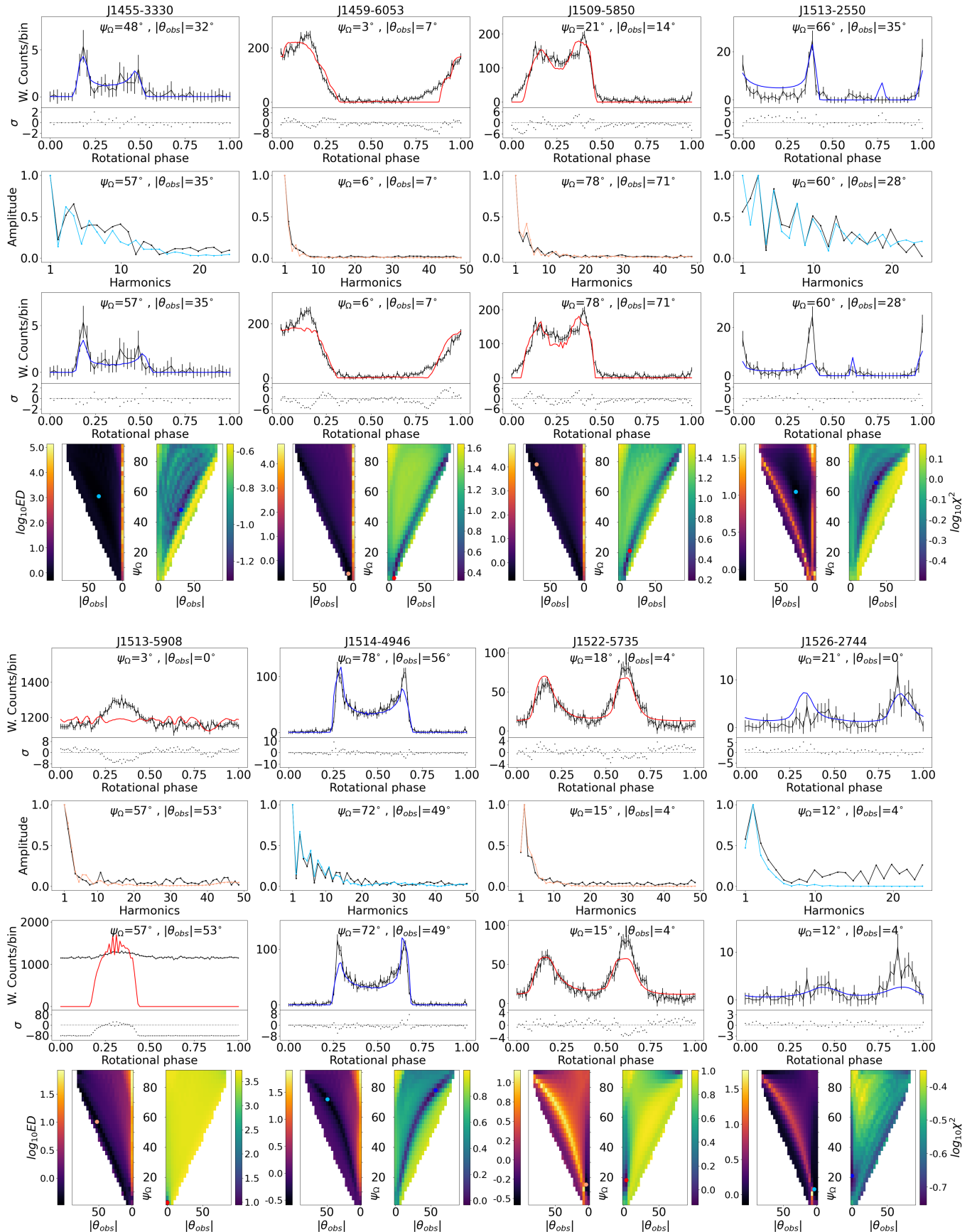


Figure C1. - continued

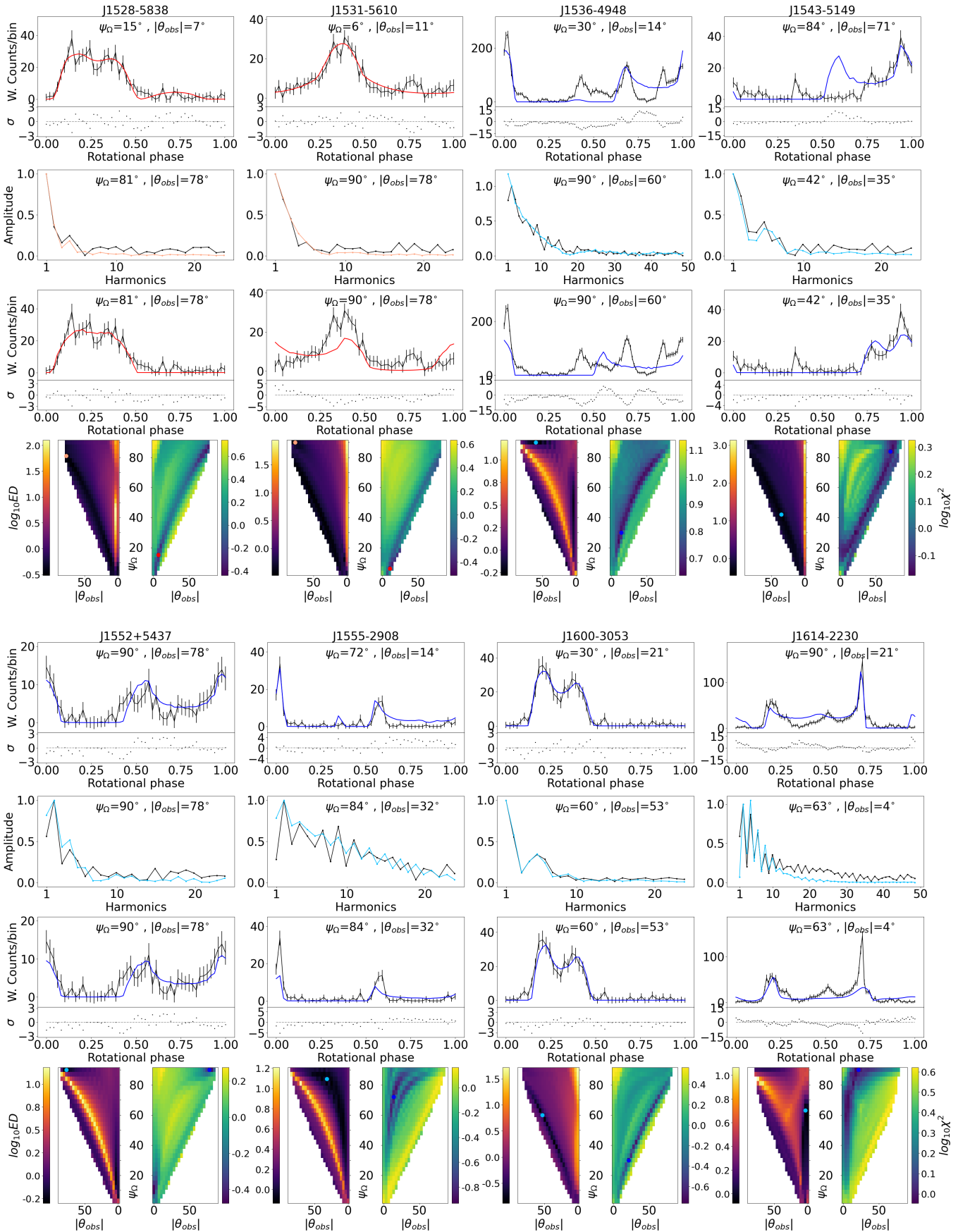


Figure C1. - continued

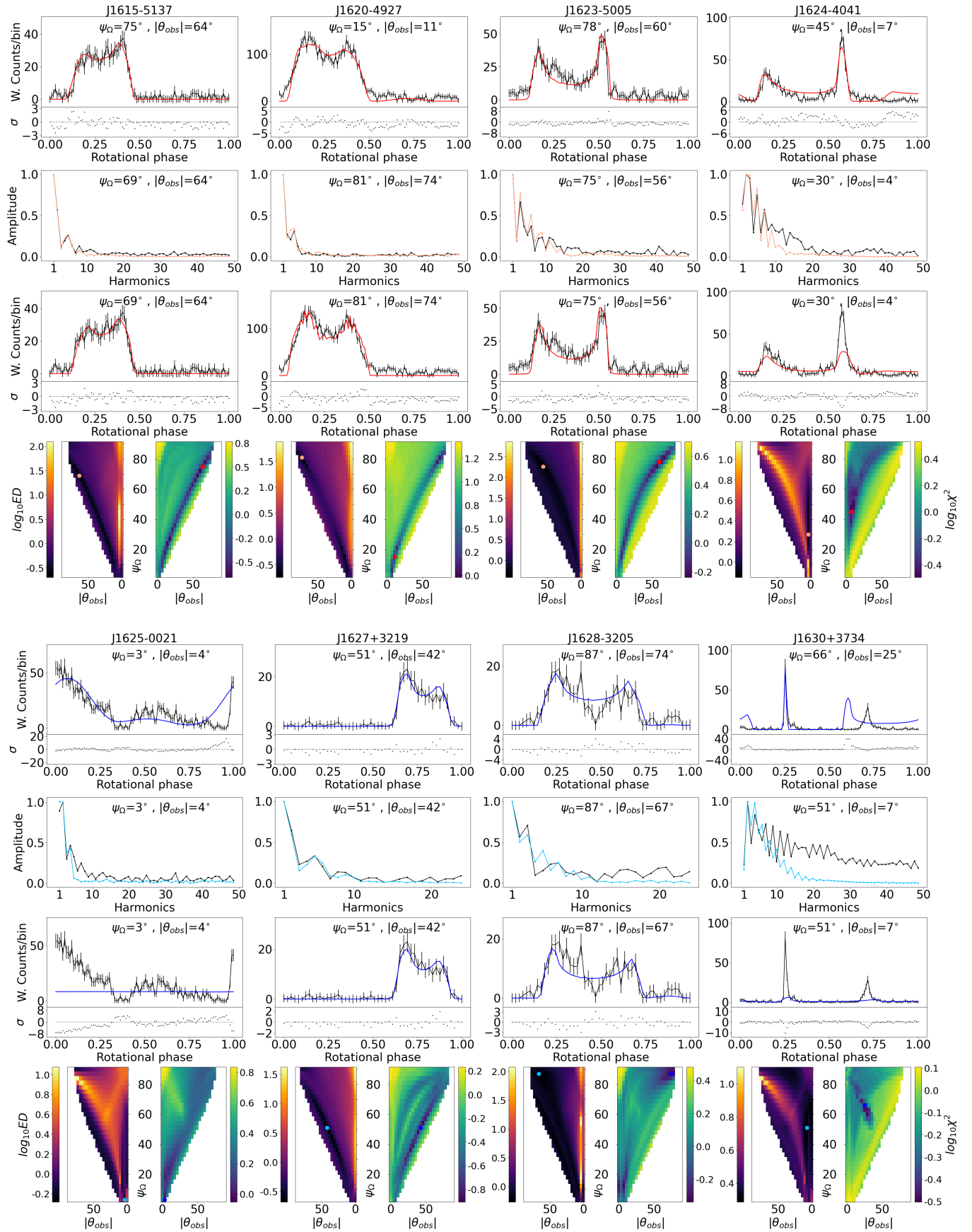


Figure C1. - continued

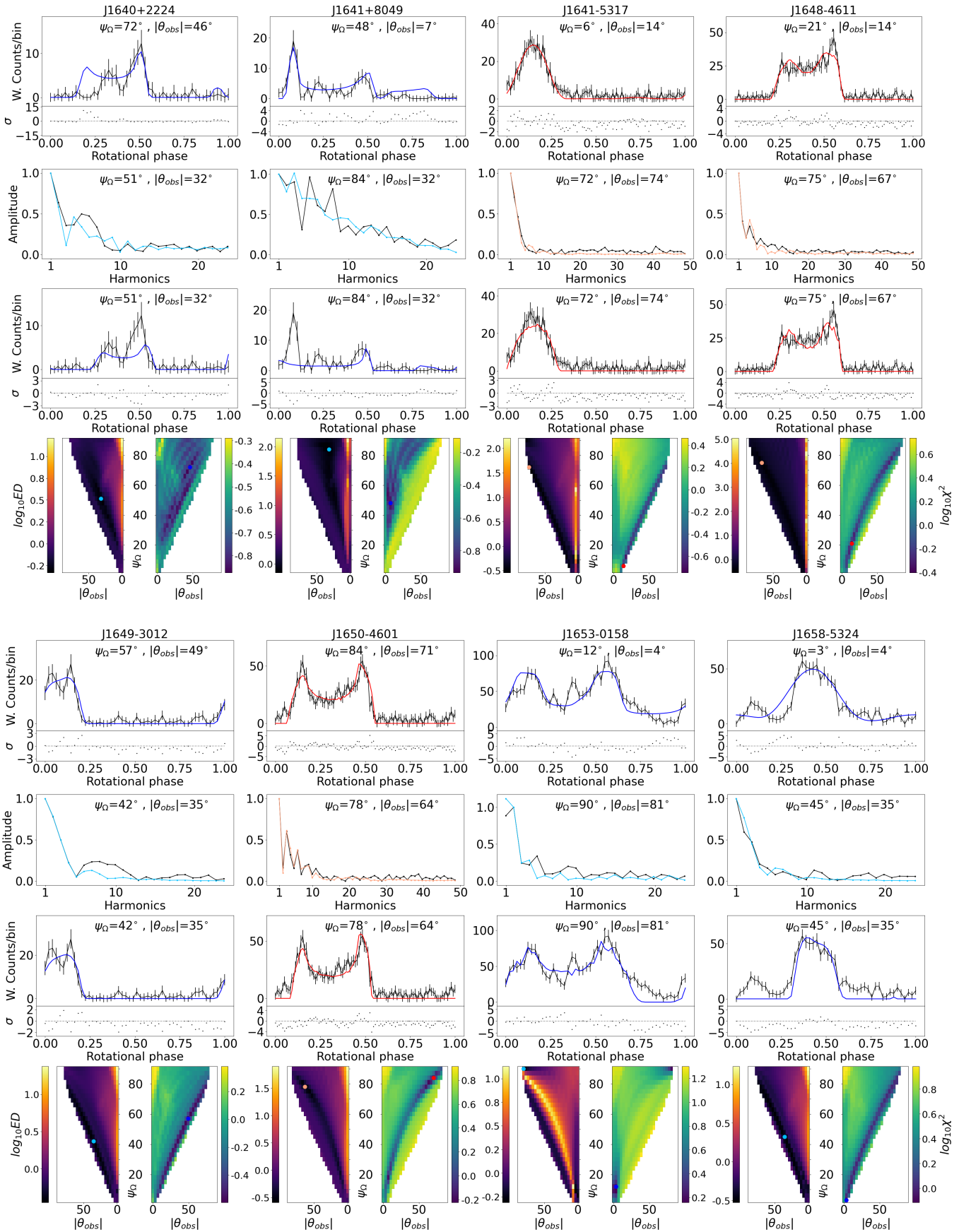


Figure C1. - continued

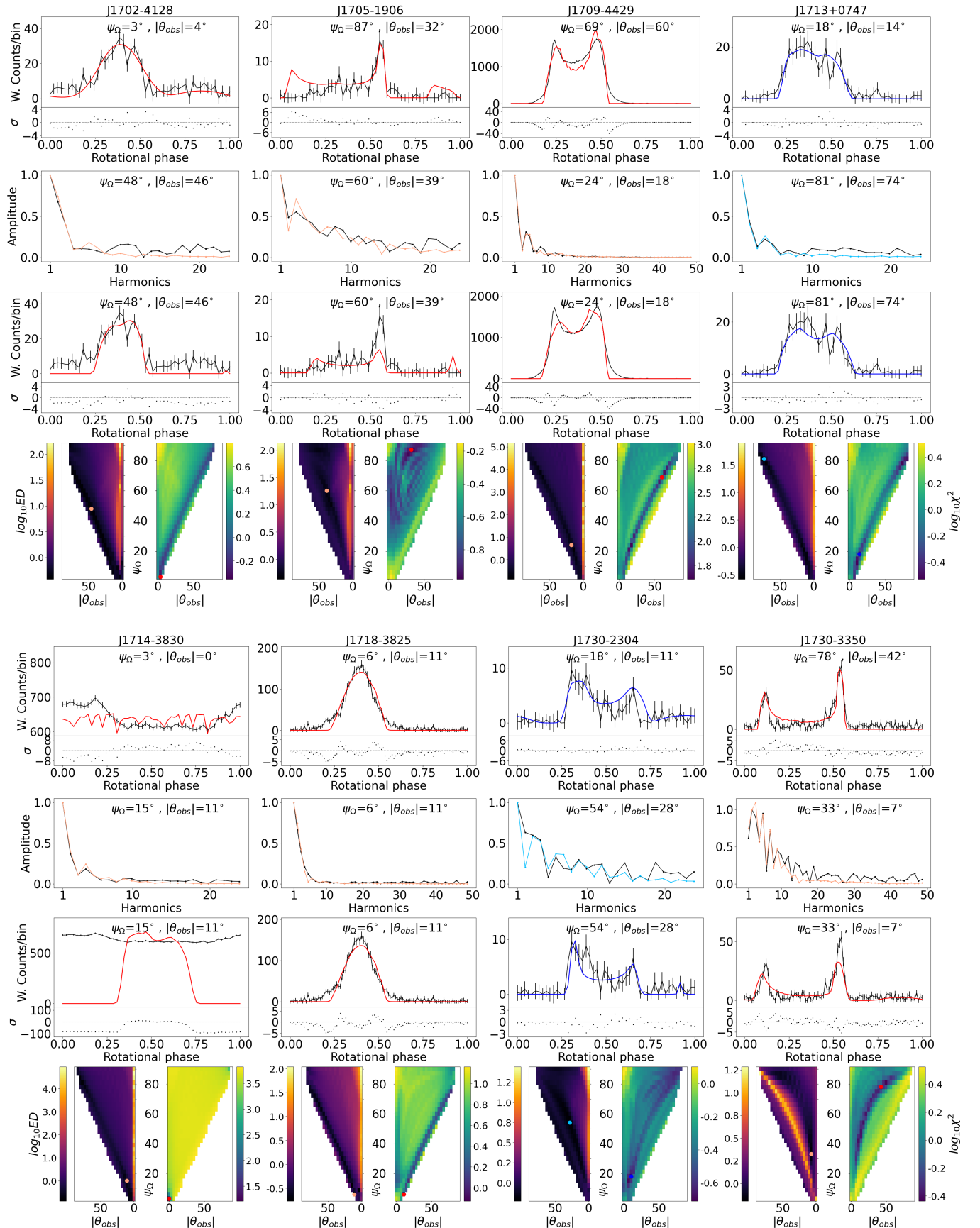


Figure C1. - continued

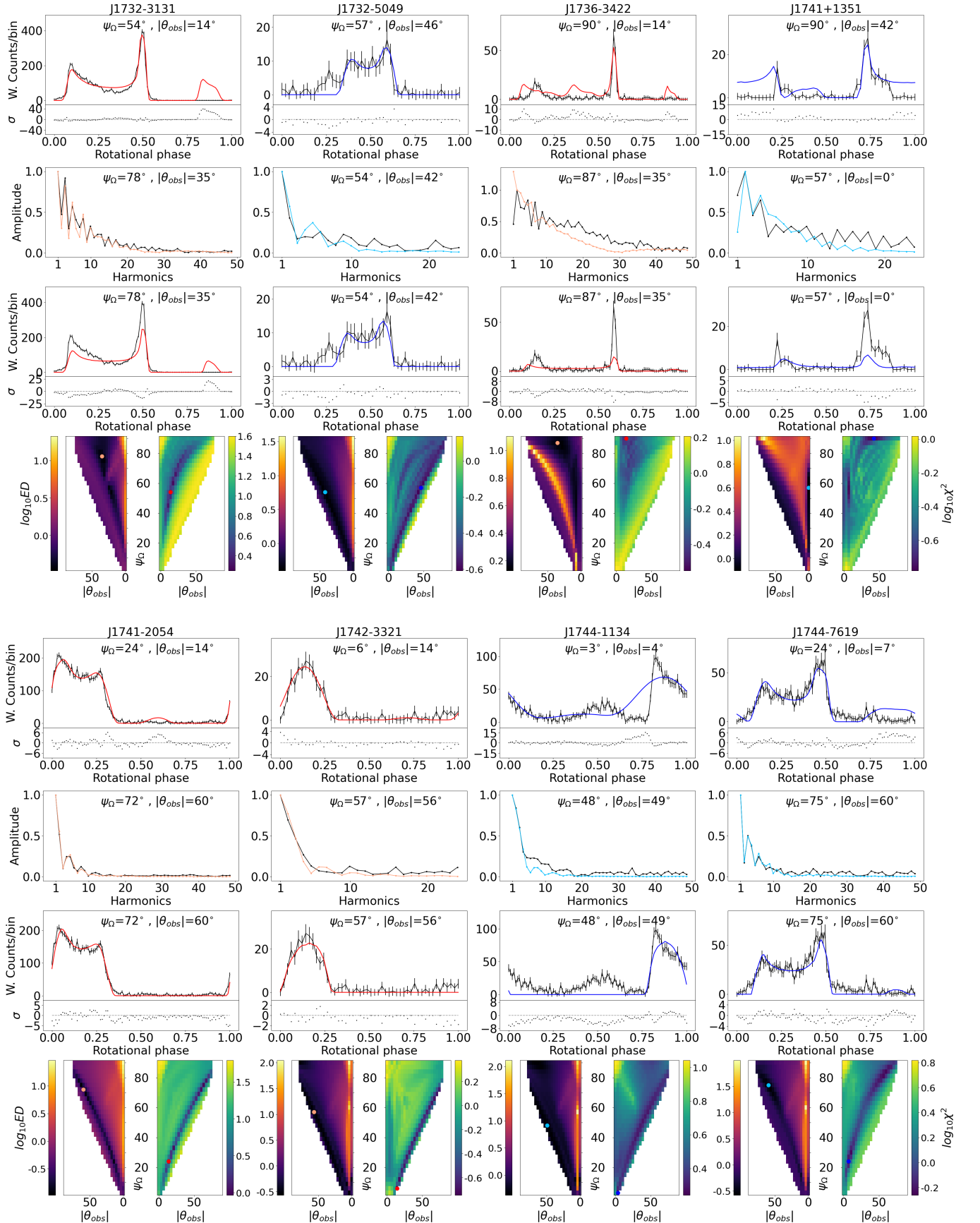


Figure C1. - continued

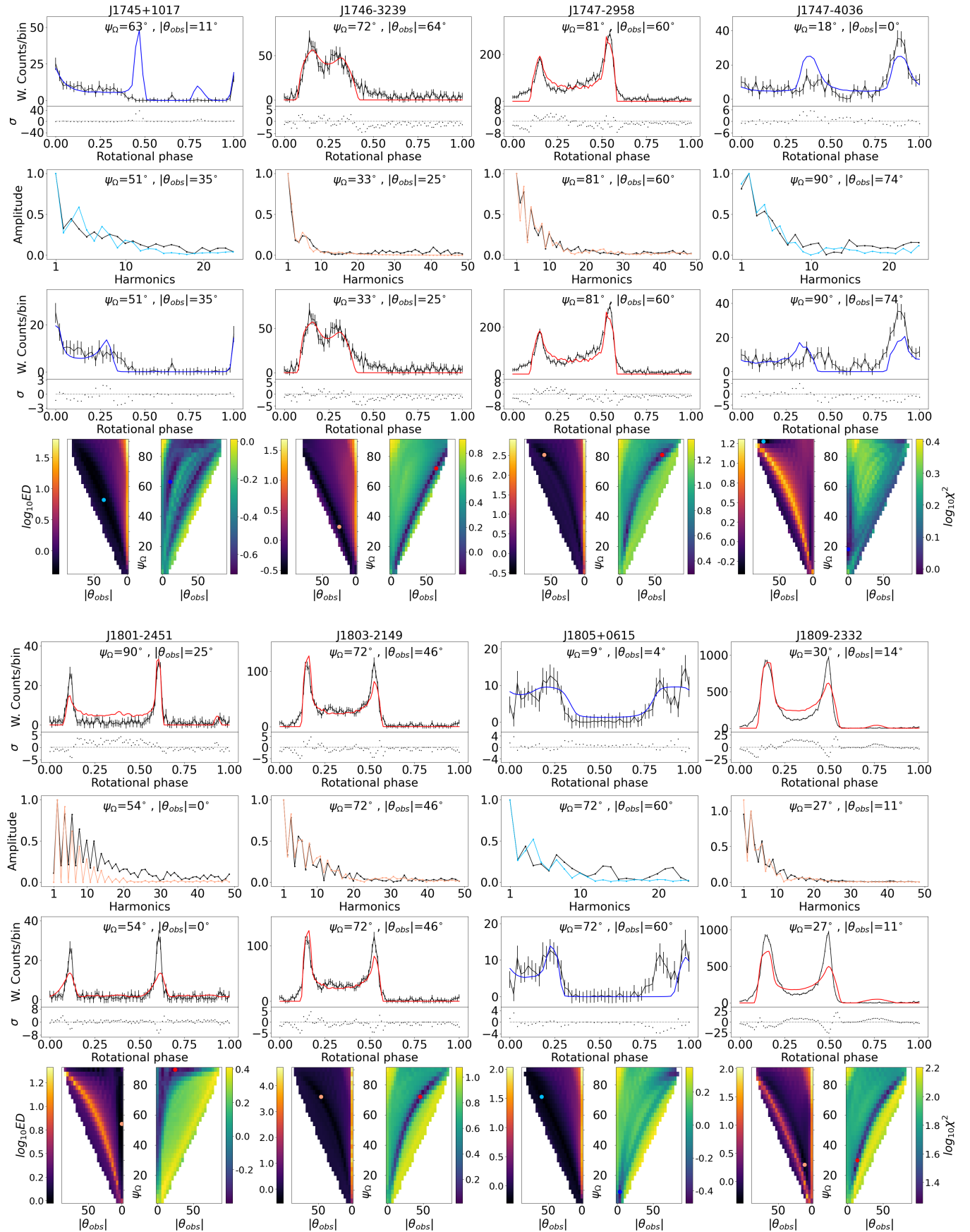


Figure C1. - continued

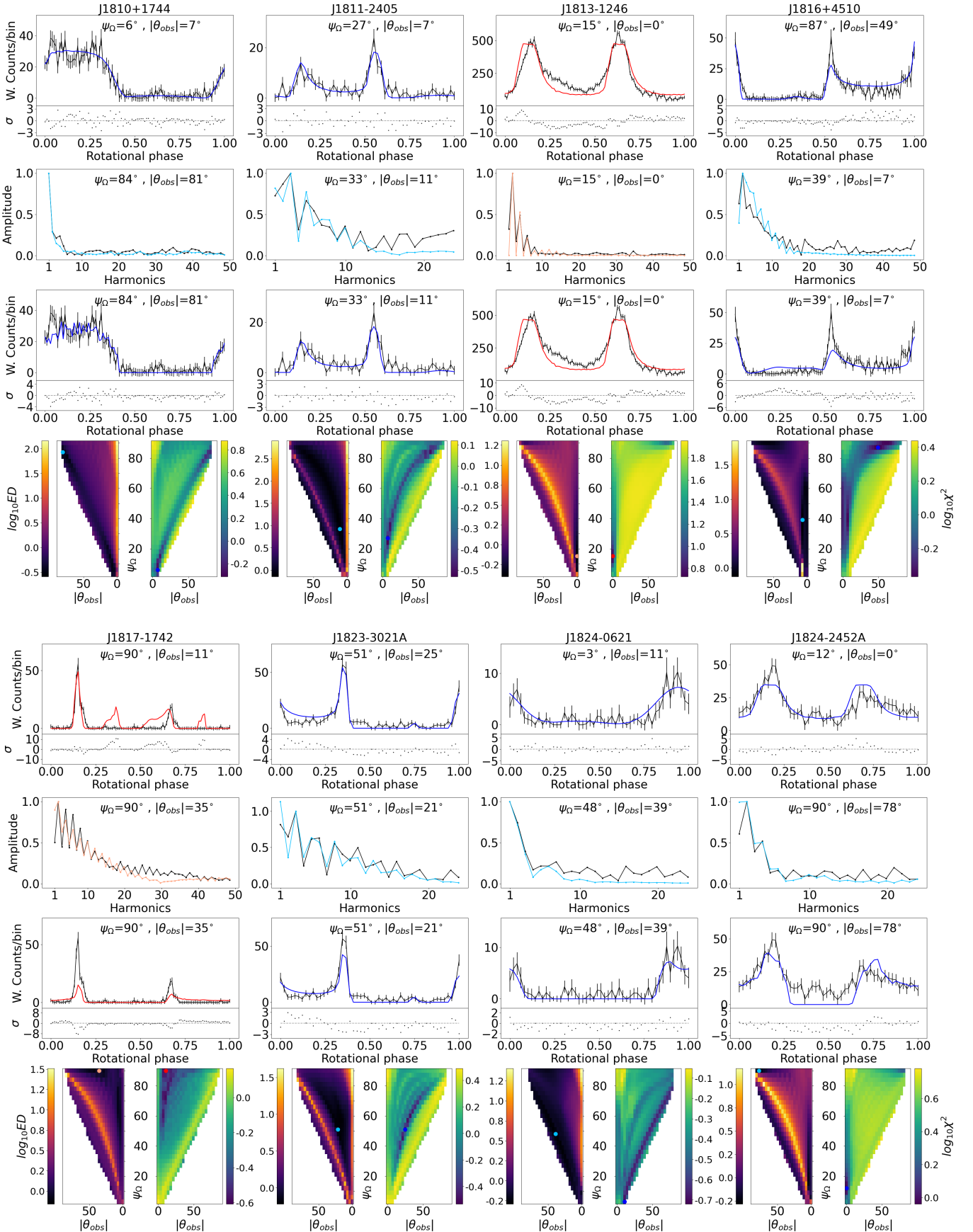


Figure C1. - continued

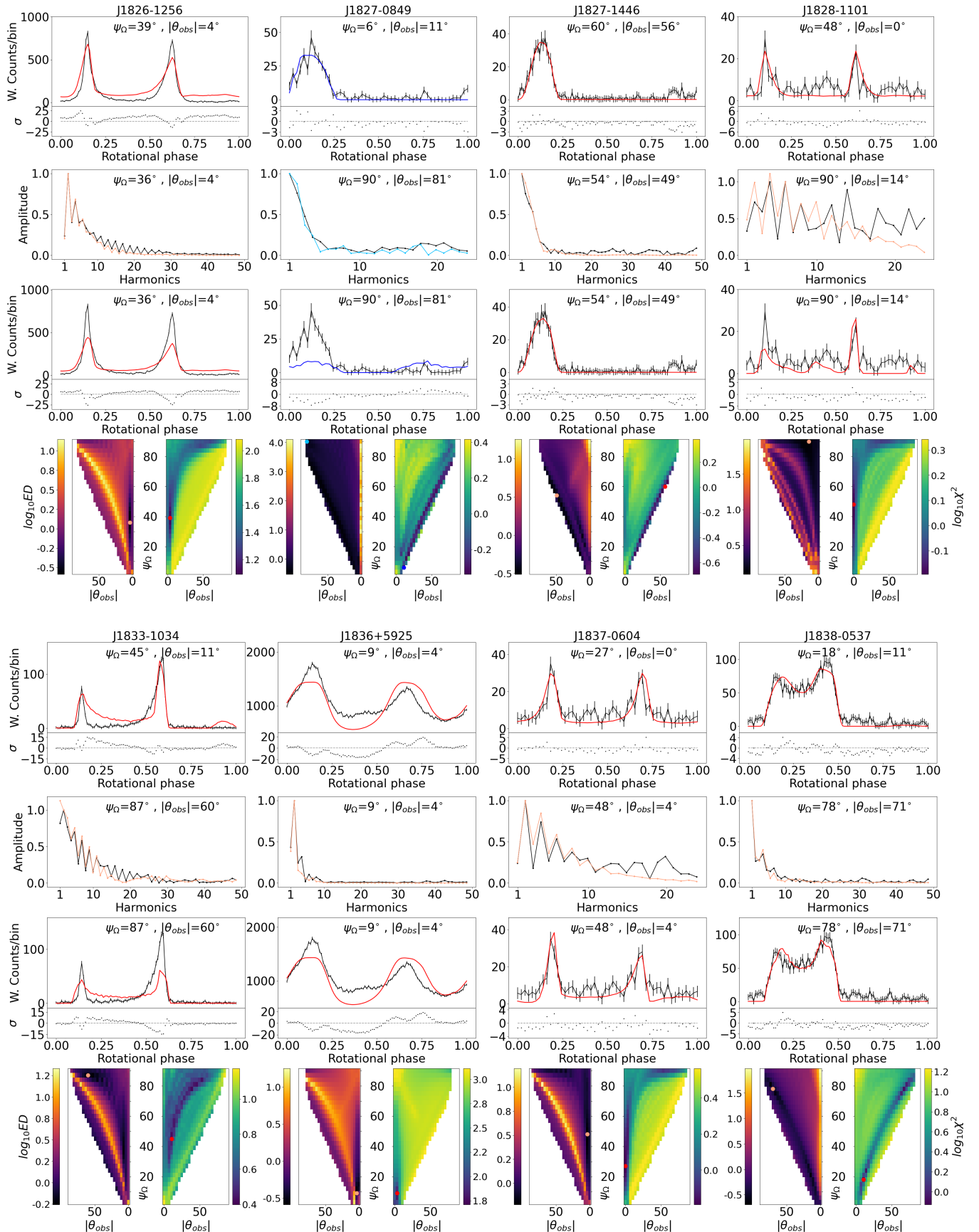


Figure C1. - continued

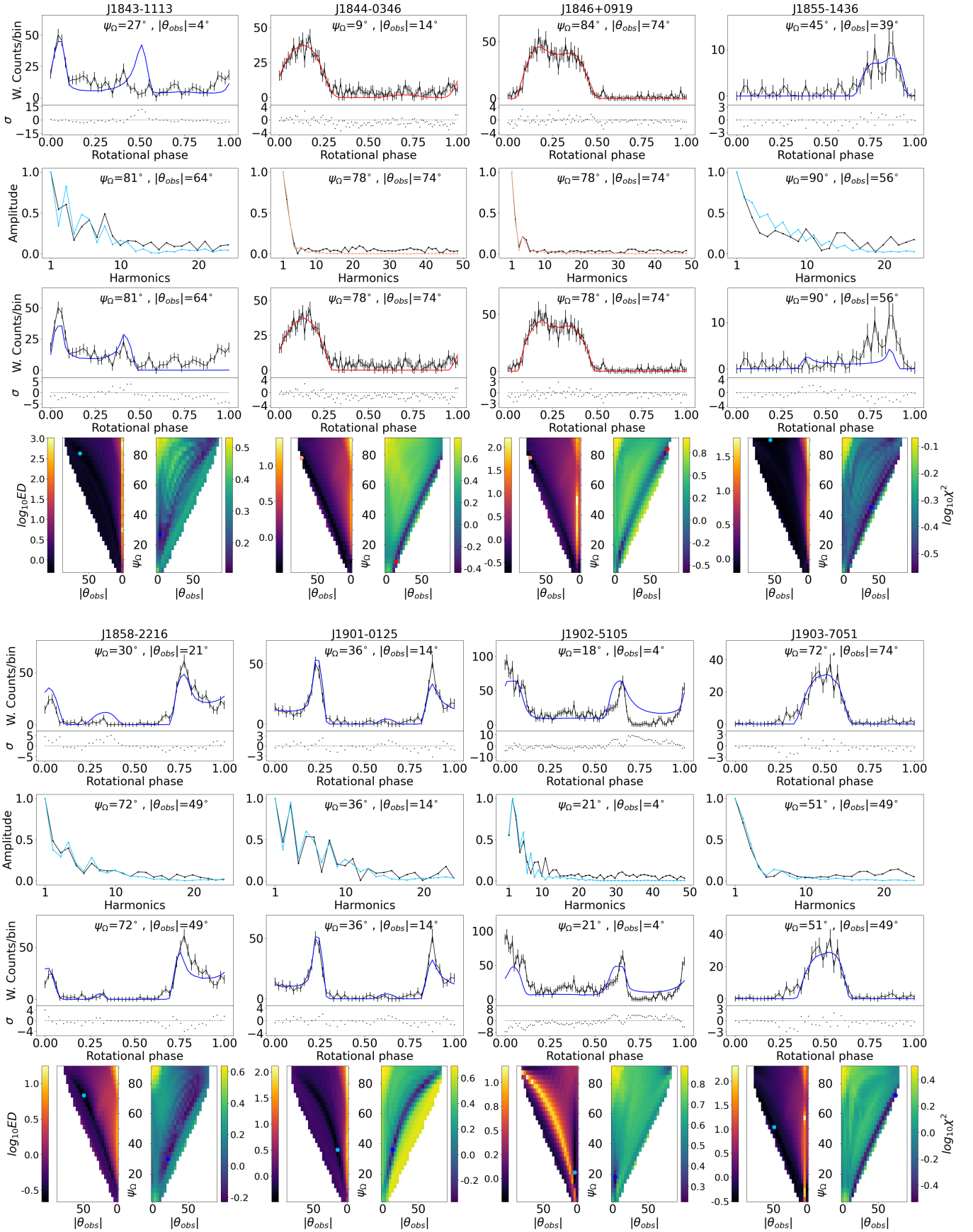


Figure C1. - continued

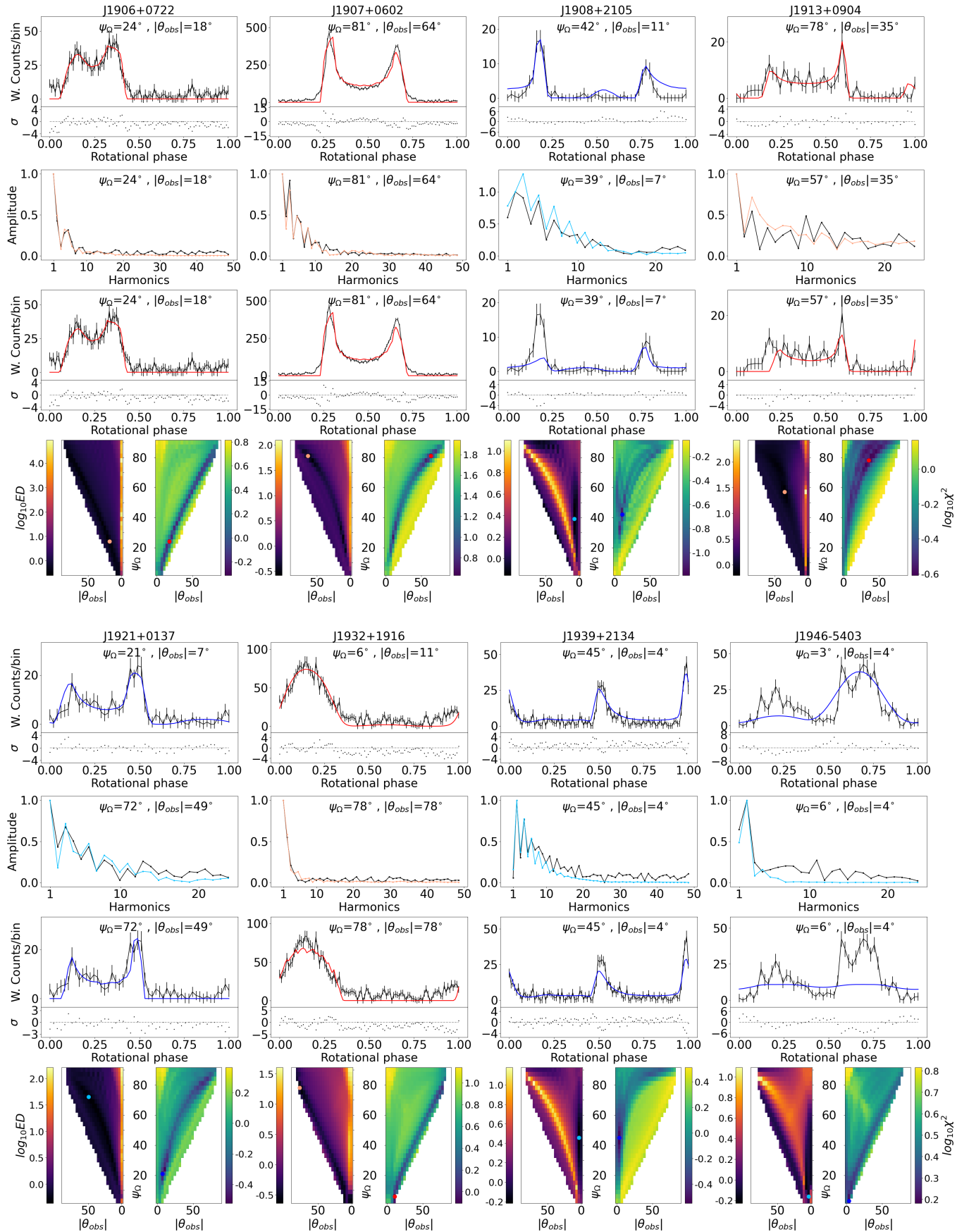


Figure C1. - continued

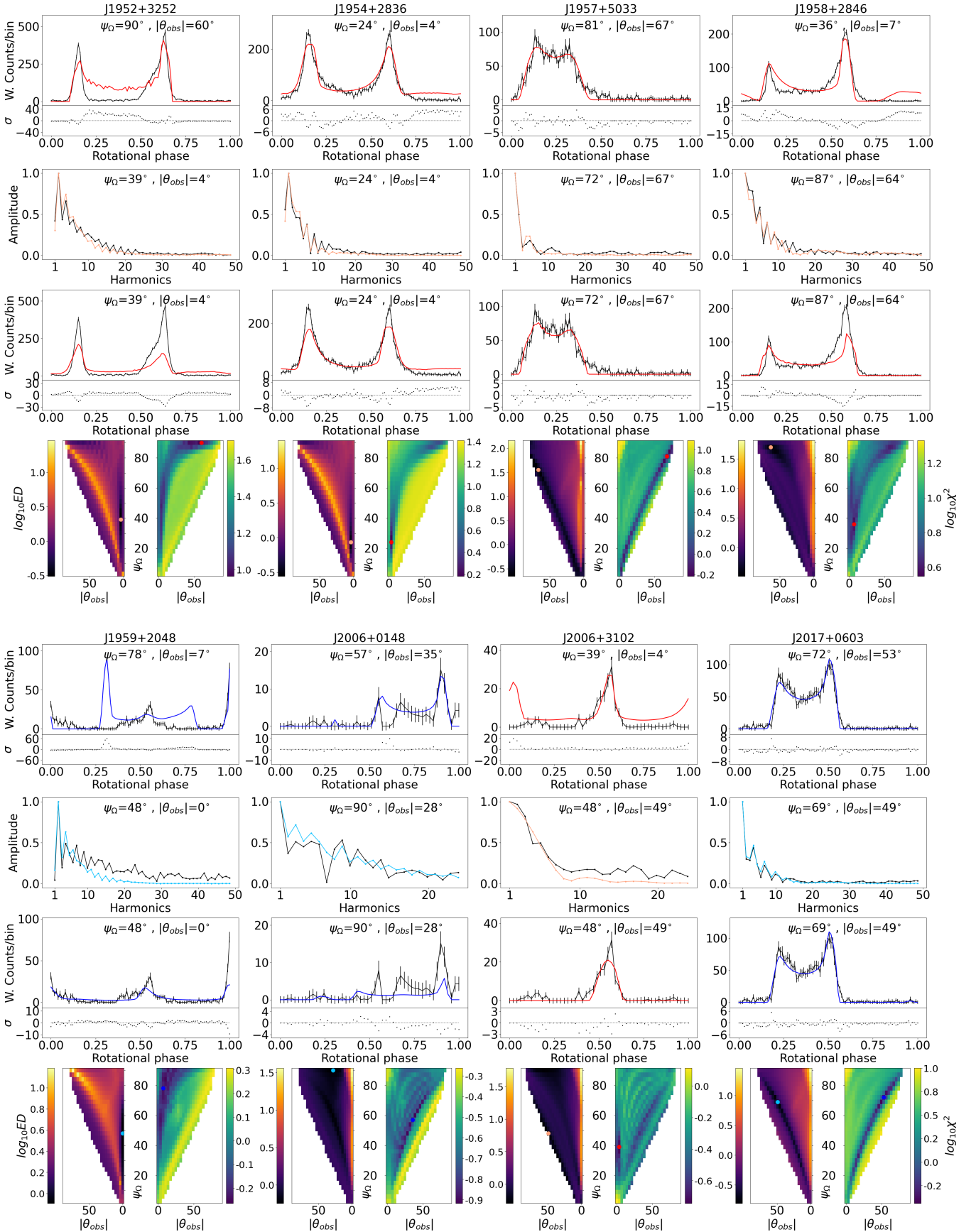


Figure C1. - continued

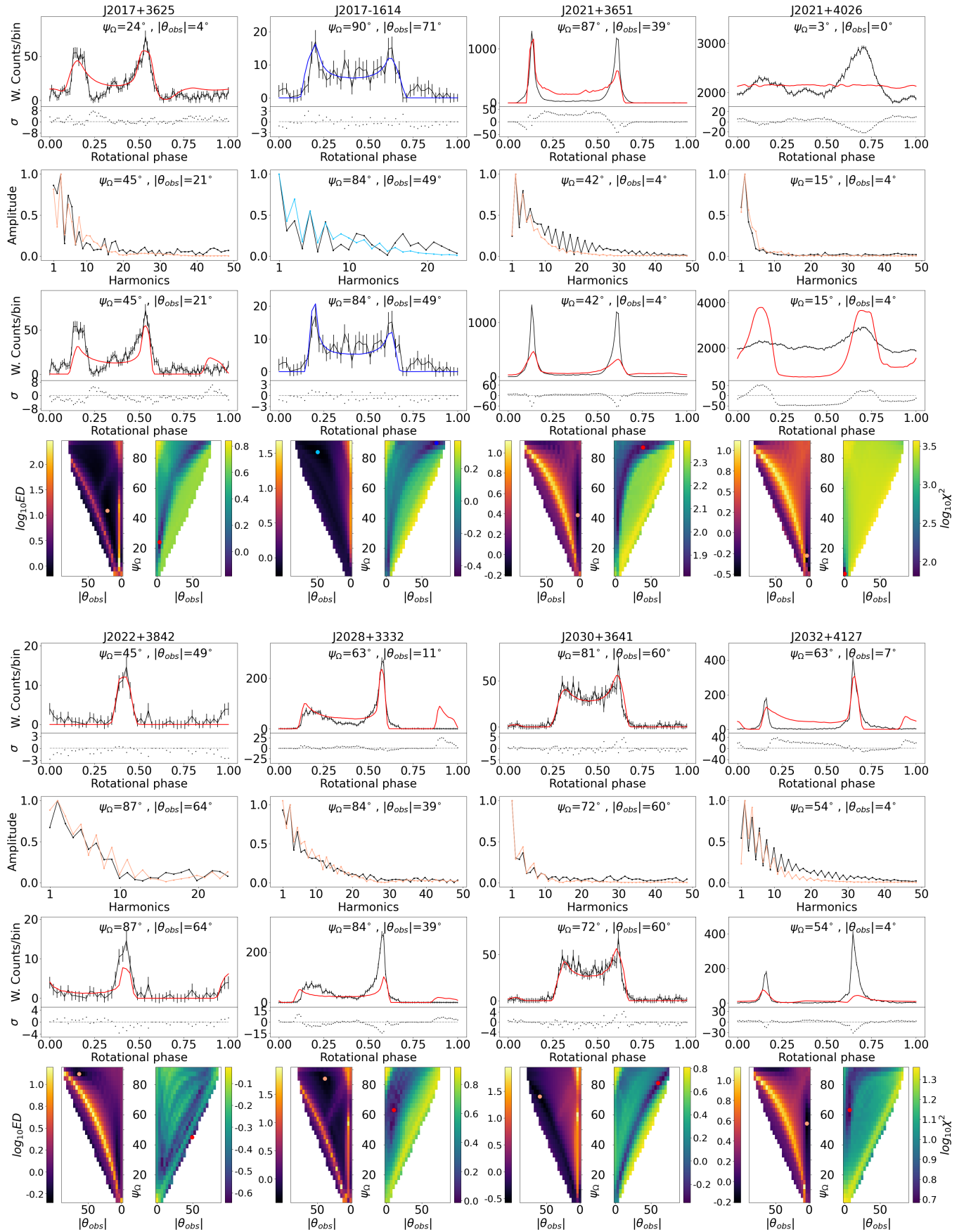


Figure C1. - continued

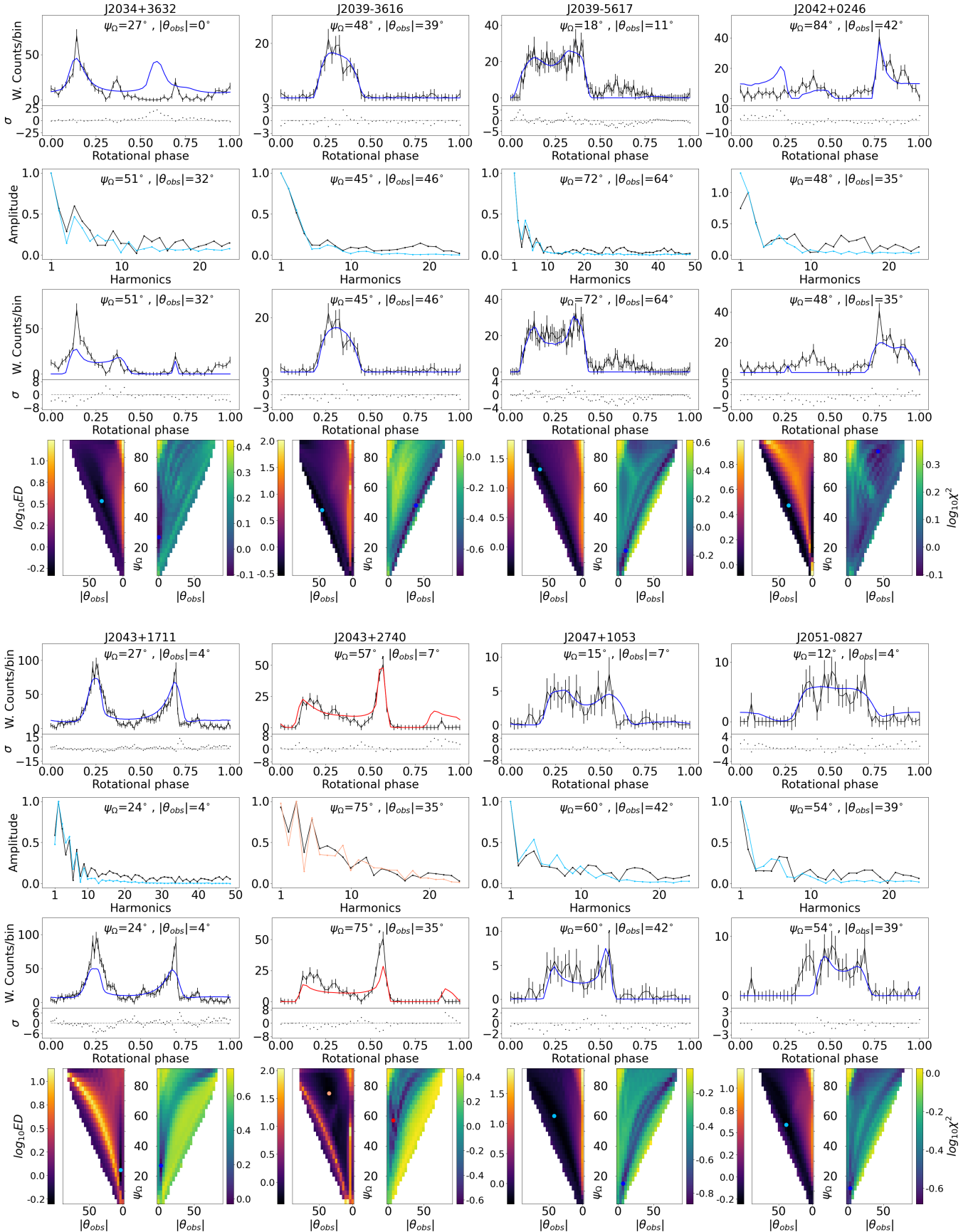


Figure C1. - continued

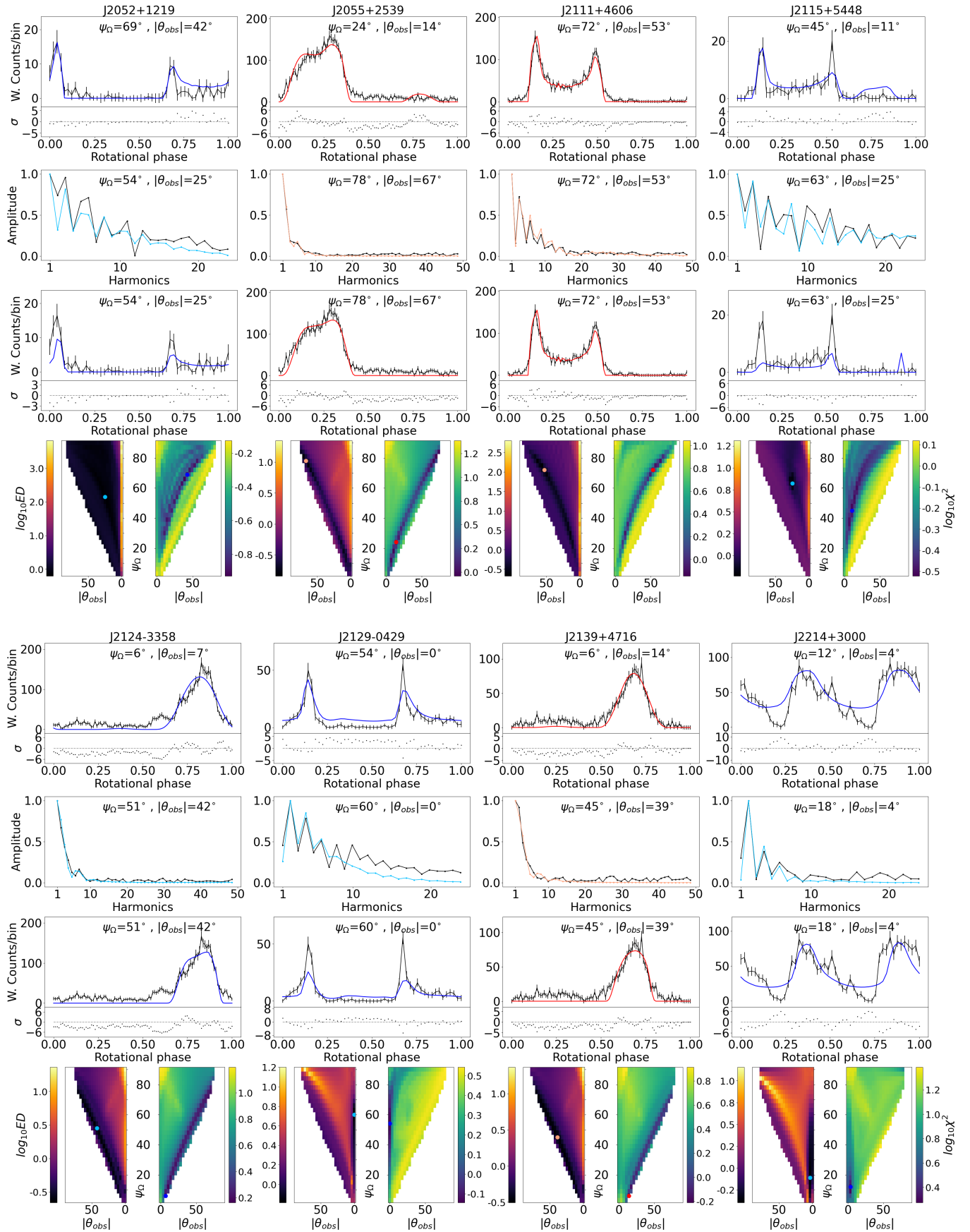


Figure C1. - continued

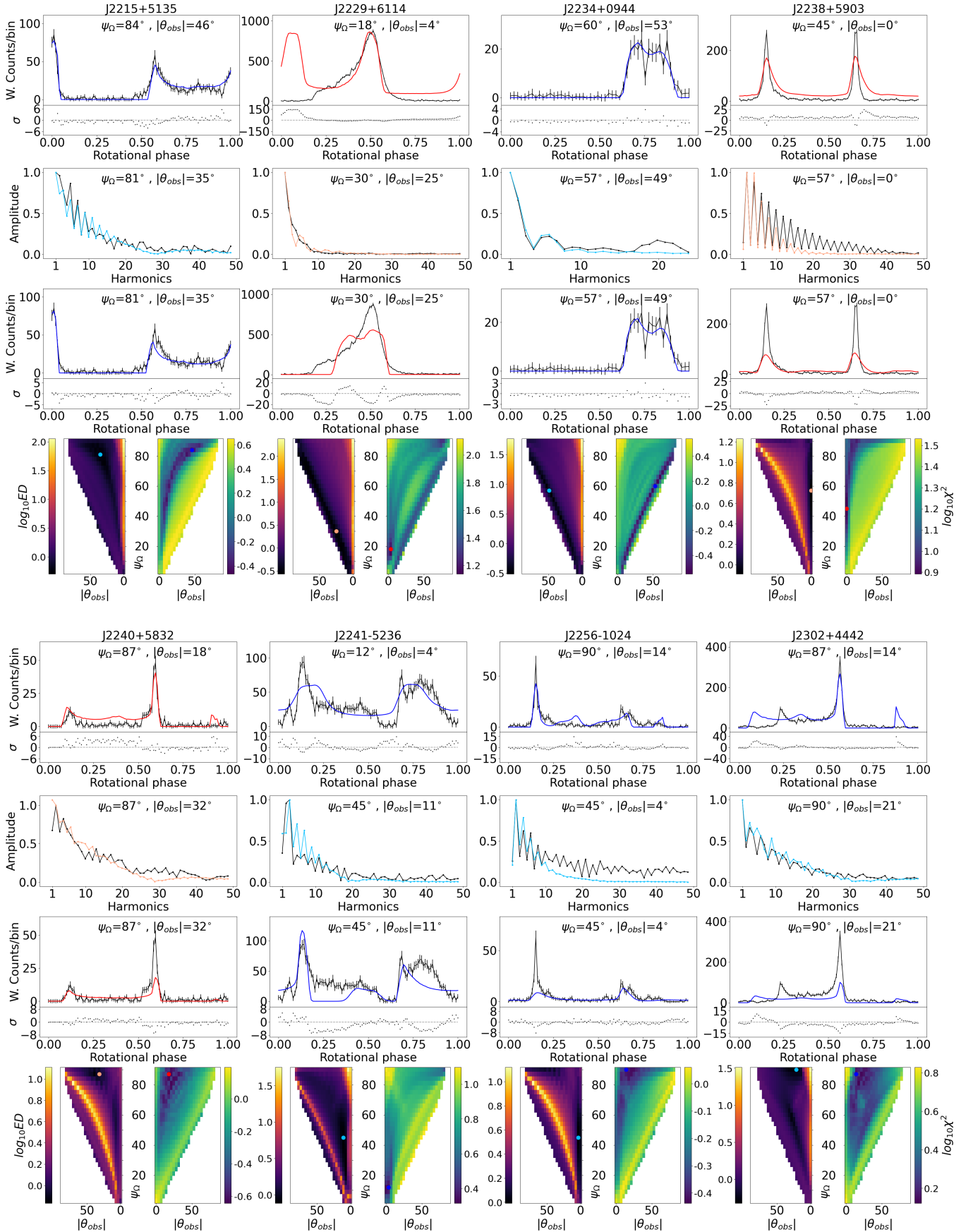


Figure C1. - continued

Table C1. - *continued*

Pulsar	Time domain		Frequency domain		Pulsar	Time domain		Frequency domain	
	$\psi_{\Omega}[^{\circ}]$	$ \theta_{obs} [^{\circ}]$	$\psi_{\Omega}[^{\circ}]$	$ \theta_{obs} [^{\circ}]$		$\psi_{\Omega}[^{\circ}]$	$ \theta_{obs} [^{\circ}]$	$\psi_{\Omega}[^{\circ}]$	$ \theta_{obs} [^{\circ}]$
J1649–3012	21	18	42	35	J1903–7051	6	14	51	49
J1650–4601	18	7	78	64	J1906+0722	24	18	24	18
J1653–0158	9	4	90	81	J1907+0602	81	64	81	64
J1658–5324	3	4	45	35	J1908+2105	30	35	39	7
J1702–4128	3	4	48	46	J1913+0904	78	53	57	35
J1705–1906	72	49	60	39	J1921+0137	24	11	72	49
J1709–4429	24	18	24	18	J1932+1916	6	11	78	78
J1713+0747	12	11	81	74	J1939+2134	45	4	45	4
J1714–3830	3	0	15	11	J1946–5403	3	4	6	4
J1718–3825	6	11	6	11	J1952+3252	42	4	39	4
J1730–2304	33	14	54	28	J1954+2836	21	4	24	4
J1730–3350	42	11	33	7	J1957+5033	84	71	72	67
J1732–3131	78	56	78	35	J1958+2846	84	56	87	64
J1732–5049	12	11	54	42	J1959+2048	48	0	48	0
J1736–3422	54	7	87	35	J2006+0148	45	32	90	28
J1741–2054	75	64	72	60	J2006+3102	15	18	48	49
J1741+1351	54	49	57	0	J2017+0603	78	64	69	49
J1742–3321	66	67	57	56	J2017+3625	24	4	45	21
J1744–1134	54	42	48	49	J2017–1614	90	71	84	49
J1744–7619	87	67	75	60	J2021+3651	48	4	42	4
J1745+1017	75	60	51	35	J2021+4026	3	0	15	4
J1746–3239	9	11	33	25	J2022+3842	33	7	87	64
J1747–2958	21	7	81	60	J2028+3332	84	64	84	39
J1747–4036	15	0	90	74	J2030+3641	84	67	72	60
J1801–2451	54	0	54	0	J2032+4127	18	25	54	4
J1803–2149	72	46	72	46	J2034+3632	3	11	51	32
J1805+0615	87	74	72	60	J2039–3616	39	39	45	46
J1809–2332	36	18	27	11	J2039–5617	12	11	72	64
J1810+1744	6	7	84	81	J2042+0246	3	4	48	35
J1811–2405	24	7	33	11	J2043+1711	21	4	24	4
J1813–1246	15	0	15	0	J2043+2740	81	53	75	35
J1816+4510	90	56	39	7	J2047+1053	69	53	60	42
J1817–1742	30	35	90	35	J2051–0827	84	64	54	39
J1823–3021A	51	25	51	21	J2052+1219	63	32	54	25
J1824–2452A	9	0	90	78	J2055+2539	12	14	78	67
J1826–1256	39	4	36	4	J2111+4606	78	64	72	53
J1827–0849	12	14	90	81	J2115+5448	75	49	63	25
J1828–1101	6	0	90	14	J2124–3358	9	7	51	42
J1824–0621	69	60	48	39	J2129–0429	90	56	60	0
J1827–1446	15	14	54	49	J2139+4716	6	14	45	39
J1833–1034	42	46	87	60	J2214+3000	18	4	18	4
J1836+5925	9	4	9	4	J2215+5135	84	46	81	35
J1837–0604	21	0	48	4	J2229+6114	9	11	30	25
J1838–0537	18	11	78	71	J2234+0944	54	46	57	49
J1843–1113	9	4	81	64	J2238+5903	54	0	57	0
J1844–0346	9	14	78	74	J2240+5832	27	32	87	32
J1846+0919	84	74	78	74	J2241–5236	12	4	45	11
J1855–1436	12	14	90	56	J2256–1024	39	0	45	4
J1858–2216	78	60	72	49	J2302+4442	60	35	90	21
J1901–0125	42	18	36	14	J2310–0555	84	53	42	4
J1902–5105	24	4	21	4	J2339–0533	75	46	78	53

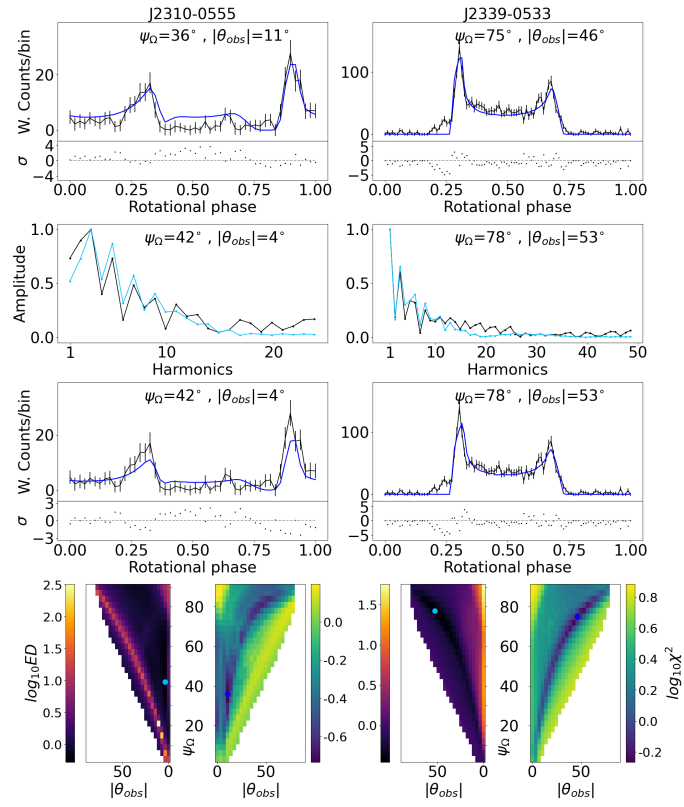


Figure C1. - continued